# THz Active Imaging Systems With Real-Time Capabilities

Fabian Friederich, *Member, IEEE*, Wolff von Spiegel, Maris Bauer, Fanzhen Meng, Mark D. Thomson, *Member, IEEE*, Sebastian Boppel, Alvydas Lisauskas, Bernd Hils, Viktor Krozer, *Senior Member, IEEE*, Andreas Keil, Torsten Löffler, Ralf Henneberger, Anna Katharina Huhn, Gunnar Spickermann, Peter Haring Bolívar, and Hartmut G. Roskos

*(Invited Paper)*

***Abstract*—This paper presents a survey of the status of five active THz imaging modalities which we have developed and investigated during the last few years with the goal to explore their potential for real-time imaging. We start out by introducing a novel waveguide-based all-electronic imaging system which operates at 812 GHz. Its salient feature is a 32-pixel linear detector array heterodyne-operated at the eighth subharmonic. This array in combination with a telescope optics for object distances of 2–6 m reaches a data acquisition speed suited for real-time imaging. The second system described then is again an all-electronic scanner (now for around 300 GHz), designed for object distances of $\geq$8 m, which combines mechanical scanning in vertical direction, synthetic-aperture image generation in horizontal direction, and frequency-modulated continuous-wave sweeping for the depth information. The third and fourth systems follow an optoelectronic approach by relying on several- to multi-pixel parallel electrooptic detection. One imager is based on a pulsed THz-OPO and homodyne detection with a CCD camera, the other on either continuous-wave electronic or femtosecond optoelectronic THz sources and a photonic-mixing device (PMD) camera. The article concludes with a description of the state of the art of imaging with focal-plane arrays based on CMOS field-effect transistors.**

***Index Terms*—Demodulating detector array, electrooptic terahertz detection, femtosecond systems, optical parametric oscillator, photonic detectors, photonic-mixer device, photonic systems, submillimeter-wave imaging, submillimeter-wave technology, synthetic-aperture imaging, synthetic-aperture radar, terahertz imaging.**

Manuscript received March 24, 2011; revised May 23, 2011; accepted May 30, 2011. Date of current version August 31, 2011. This work was supported by numerous sources, including the Federal Ministry of Education and Research Germany (BMBF) through Projects LYNKEUS, TERACAM, TEKZAS, and LiveDetect3D, by the German Research Foundation (DFG) through PAK-73 "Dynamisches 3-D Sehen mit PMD", by the European Space Agency ESA/ESTEC under Contract 21155/07/NL/ST, by WI Bank Hessen, and by Oerlikon AG.

F. Friederich, W. von Spiegel, M. Bauer, F. Meng, M. D. Thomson, S. Boppel, A. Lisauskas, B. Hils, V. Krozer, and H. G. Roskos are with the Physikalische Institut, Johann Wolfgang Goethe-Universität, 60438 Frankfurt am Main, Germany (e-mail: roskos@physik.uni-frankfurt.de).

A. Keil and T. Löffler are with SynView GmbH, 61348 Bad Homburg, Germany.

R. Henneberger is with Radiometer Physics GmbH, 53340 Meckenheim, Germany.

A. K. Huhn, G. Spickermann, and P. H. Bolívar are with the Institut für Höchstfrequenztechnik und Quantenelektronik, Universität Siegen, 57068 Siegen, Germany.

Color versions of one or more of the figures in this paper are available online at http://ieeexplore.ieee.org.

Digital Object Identifier 10.1109/TTHZ.2011.2159559

## I. Introduction

IMAGING with electromagnetic radiation in the THz frequency regime (whose lower bounds we understand here to be 300 GHz) has made considerable progress in recent years. THz imaging and sensing is being investigated and found to be promising for a plethora of applications, both in science and beyond, such as security and safety screening, process monitoring and non-contact materials testing, biological, medical and pharmaceutical analysis, etc. [1]–[11].

For many application areas, it is indispensable to generate images with a high frame-rate. Imaging at video rates or close to it is certainly necessary for many tasks concerning industrial on-line process monitoring. Frame-rates on the level of at least one frame per second are required for security screening or in the medical field, if living people are scanned.

It appears fair to state that the route to active real-time imaging is via multi-pixel parallel detection of the radiation. Much work has been devoted in recent years to develop such parallel detection schemes. Progress hinges to a considerable degree on advances in the available power of emitters and the sensitivity of detectors, but not only on these. Also system integration, the optimization of the interplay of emitters, sources, and optics, plays an important role.

Outstanding examples of dedicated work toward high-frame-rate imaging include the development of all-electronic scanners for standoff threat detection [12], [13]. But also the optoelectronic side of THz technology has seen remarkable progress, such as the realization of integrated line arrays of photoconductive and electrooptic (EO) detectors suitable for parallel readout [14], [15]. It is hoped that standoff imaging can be combined with standoff spectroscopic analysis of remotely located objects [1], [16]–[18].

This paper describes and summarizes several approaches towards real-time imaging which we have investigated in recent years. This includes all-electronic imaging, hybrid imaging—with a microelectronic emitter and laser-based EO readout—and all-optical imaging. We should state here, that we have focused only on actively illuminating imaging systems. We also have left approaches unconsidered which require cryogenic cooling of detectors (especially superconducting ones) and of emitters (such as THz quantum-cascade lasers),

because we believe that there is only a limited acceptance of such cooling outside of laboratory environments.

The paper is organized as follows. Section II describes our work on all-electronic multi-pixel imaging systems, distinguishing between mechanically scanning systems and the synthetic-aperture approach. Section III then explores two alternative optoelectronic concepts which employ conversion of the THz image data to the near-infrared spectral region. This then allows to use commercial silicon-based cameras—a CCD camera or a special time-of-flight camera—for detection. In the last part, Section IV, we address the monolithic integration of THz detectors to create focal-plane arrays (FPAs). Emphasis lies on the use of silicon MOSFETs operated as distributed resistive mixers.

## II. Active Electronic Imaging Systems

### A. Mechanically Scanning Imaging Systems

This section focuses on bringing fully electronic THz imaging with high-performance waveguide-based components towards video-rate operation. The first fully electronic THz-imaging system, which we realized, utilized a single emitter and single detector, operating at 620 GHz, and $x$–$y$ scanning by linear translation stages. The data acquisition time of several minutes was clearly limited by the mechanical scanning process. By switching from translational scanning to two-axes rotational scanning, we reduced the acquisition time for an image to 9 s [19]–[21]. With a frequency-agile emitter-detector combination [12], this system was also extended to range-resolving capabilities employing the frequency-modulated continuous-wave (FMCW) concept [22], [23]. We come back to it at the end of this section.

Fig. 1 displays a 620-GHz image of a handgun taken with this rotational-scanning system (without range resolution) [20]. The barrel is not visible, because the specularly reflected beam returning from it misses the aperture of the optics and hence does not reach the detector. With minor changes to the software, the image generation time could be reduced further to 1.25 s, then being limited by the maximum angular velocity of the rotational stage ($8°/s$). Further speed improvements should be possible by employing a faster rotational stage, but the approach would reach mechanical limits, before it could get close to video rates. Apart from the high angular velocities, the integration time available for each pixel would also become a limiting factor for the system's performance.

Both the mechanical problems and those concerning signal averaging can be alleviated by employing multiple detectors (and/or multiple sources). Since waveguide-based components are expensive, especially for high frequencies ($>0.3$ THz), the costs set a limit for the number of elements, and 2-D arrays with one detector for each pixel are not an option with this technology today. A good alternative are line scanners. 2-D images are generated either by exploiting the motion of the object (e.g., in the case of production lines or transport belts) or by active scanning.

We realized an explorative imaging system with a single emitter and 32 detectors for a radiation frequency of 812 GHz. The detectors are arranged in a line, and images are acquired by


Fig. 1. Photograph and 620-GHz image of a handgun. The latter taken with a single-pixel scanner from a distance of about 0.5 m. The measuring time was 9 s. The gray-scale bar shows the IF power level detected by the lock-in-amplifier in dBm. The length of the weapon from hammer to muzzle is 15 cm. Typically, 50 000 data points are acquired in the field of view. They are binned to about 10 000 points, which serve as nodes on a triangular mesh to render an image with regular pixel spacing.

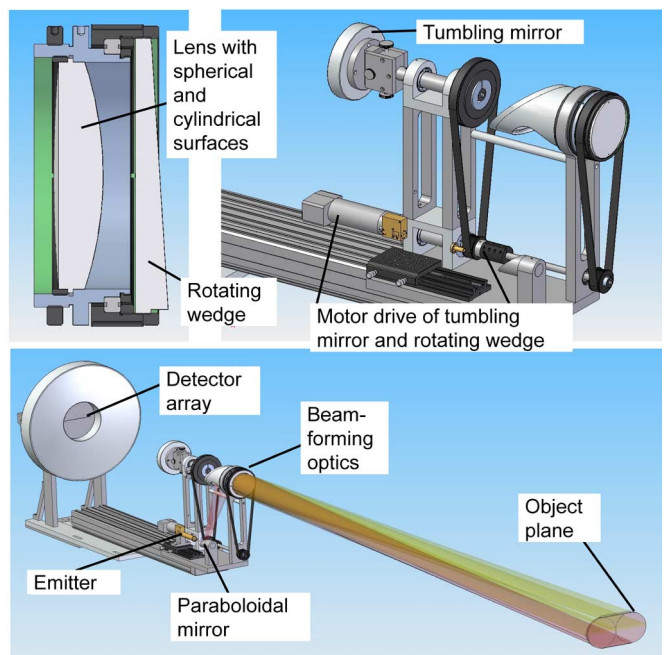


Fig. 2. Reflective 812-GHz real-time line scanner. Bottom panel: Total view, with the THz beam focused to a line and moved such that it illuminates a race-track-shaped section of the object plane. Top right: Frontal part of the system showing the motor-driven tumbling mirror at the back and the beam-forming optics of the illumination with the motor-driven wedged plate in the front. The emitter is placed at the bottom in the middle part of the display (brass-colored object, color online). Top left: Cross section through beam-forming optics.

means of a single rotating mirror. Fig. 2 displays CAD representations of the setup. The panel at the bottom displays a view of the whole system, the salient features being the telescope optics and the illumination beam. The system contains two motor-driven units (see upper right panel of Fig. 2) rotating at the frame-rate of about 10 Hz: a wedged plate being part of the beam-forming optics of the illumination, and the secondary mirror of the telescope. Both motions are synchronized to each other.

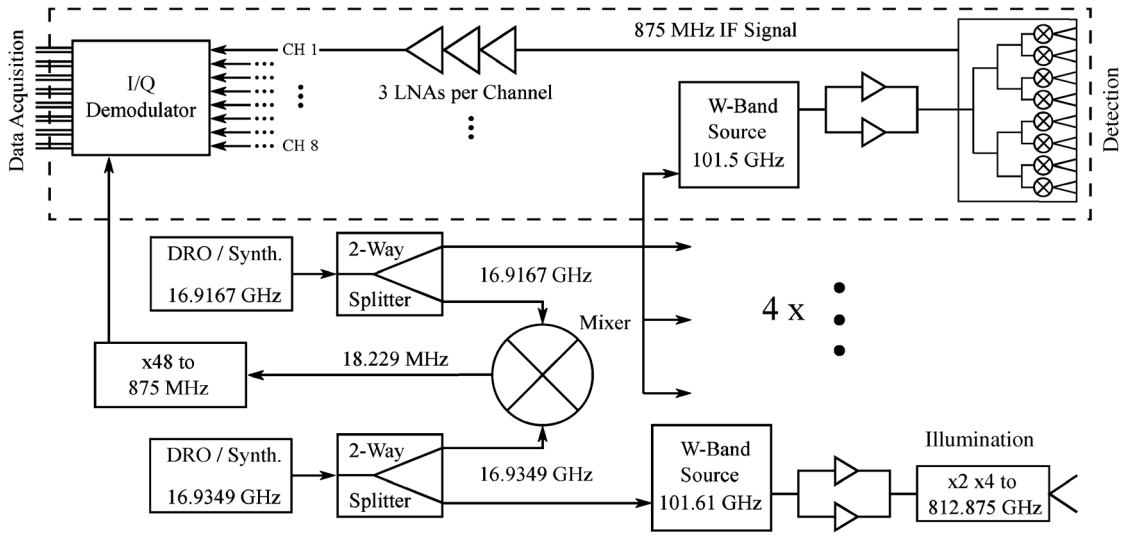


Fig. 3. Schematic representation of the electronics of the 812-GHz imaging system.

The first generates a linear illumination pattern of the emitter's radiation in the object plane, 4 m away from the primary mirror. The illumination line keeps its horizontal orientation while each point of the line moves along a circular path in the object plane. The radius of the circle is 7.5 cm in a distance of 4 m, which results in a race-track-shaped illuminated area covering approximately $13 \times 26$ cm$^2$. The synchronous motion of the secondary mirror ensures, that the illuminated section of the object plane is imaged onto the linear 32-channel receiver array which is located in the central bore of the large primary mirror of the telescope.

The telescope's quasi-optics consist of two rotationally symmetric mirrors designed for diffraction-limited standoff imaging at an adjustable distance between 2 and 6 m. For a working distance of 4 m, the numerical aperture of the optics is 0.06. The aspherical primary mirror has a diameter of 480 mm and a radius of curvature at the center of 1373 mm, the rotating secondary mirror is also aspherical, has a diameter of 140 mm, and a radius of curvature at the center of 393 mm. The secondary mirror is tilted with an adjustable angle with respect to its rotational axis in order to produce a tumbling motion. Extra weights mounted on its shaft cancel moments of torque and ensure dynamic balancing.

Considering the limited radiation power available from the source, we refrained from illumination of the whole scene in the object plane to be imaged, but rather implemented the synchronized line illumination addressed above. The upper left panel of Fig. 2 illustrates the implementation of the beam-forming optics. The THz beam is shaped by a single-element lens with a convex spherical surface on one side and a concave cylindrical surface on the other. The scanning is realized by a beam-steering wedge, which rotates in synchronicity with the secondary mirror of the imaging telescope, both driven by the same motor. The angle of the wedge is selected corresponding to the desired working distance. Two different wedges for imaging distances of 2 and 4 m were realized. The lens and the rotating wedge are homemade from high-density polyethylene (HDPE) via CNC-machining.

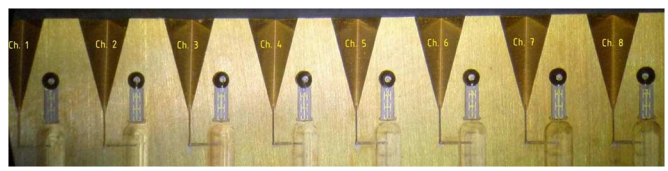


Fig. 4. View into one of the eight-channel 812-GHz receiver blocks. The spacing of the channels is 4 mm. THz radiation impinging from the top onto a horn antenna and guided into the block by a L-shaped waveguide is mixed with the local-oscillator signal arriving in the waveguide at the bottom. The intermediate-frequency signal is extracted through a coaxial waveguide seen next to the horn antenna.

The detector array, located in the central bore of the main mirror, consists of four brass blocks each containing eight detector channels. Fig. 4 shows a view into one of the blocks, opened to display its inner structure. The detectors are heterodyne receivers operating at the eighth subharmonic.

Fig. 3 presents the layout of the electronics of the system. The lower part represents the power generation chain. It starts with a synthesizer controlled by a dielectric resonator oscillator (DRO). The output signal is split, one part being used for the intermediate-frequency (IF) reference generation chain, the other for the radiation source. The latter part is fed to a multiplier chain, with power splitting, amplification and recombination in the $W$-band, followed by frequency doubling and then quadrupling to finally obtain the 812-GHz radiation used for active illumination.

The radiation frequency was chosen as a compromise between optimal spatial resolution and the limits of radiation-power generation. At 812 GHz, power levels of 1 mW appear feasible (albeit challenging). Diffraction, on the other hand, does not yet limit the resolution very severely, the spatial resolution in 4 m distance being 7.5 mm, which still allows to obtain fairly detailed images of security-relevant objects. Issues of penetration through clothing and other materials certainly have to be considered also [24].

The upper part of Fig. 3 sketches the detector electronics. The detectors are heterodyne receivers with subharmonic mixers.

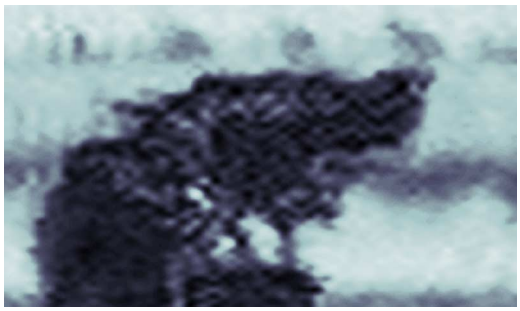

Fig. 5. Captured image from the real-time line scanner with a source power of less than 40 $\mu$W. Reflection image of the handgun of Fig. 1, positioned 4 m in front of the primary mirror. The image is a composition of several measurements, since only a small group of connected detectors with full performance was available. Their data, taken at different horizontal object positions, were combined to this image.

The local-oscillator (LO) signal is provided by one $W$-band source per each of the four detector modules, the sources being driven by a common DRO synthesizer. The output power of each $W$-band source is amplified in two stages and split three times in order to provide each detector with sufficient LO power (about 12 dBm per pixel). The LO signal, at 101.5 GHz, is then mixed with the incoming THz radiation, generating an IF signal at the 8th harmonic of the LO signal minus the frequency of the THz wave. The IF is about 875 MHz, given by the difference frequency of the two DROs multiplied by the factor of 48. The DROs are not locked to each other, which results in slight IF drifts. The IF signal of each channel is amplified by three low-noise amplifiers, and then I/Q demodulated (I/Q: in-phase/quadrature). The resulting 64 low-frequency signals for the in-phase and quadrature components are low-pass-filtered and fed into the data acquisition unit for digitization and image generation on a PC.

The central part of Fig. 3 shows that the IF reference signal for the I/Q demodulator is generated by multiplying the difference frequency of the two synthesizers by the factor of 48. Any IF drift is hence present also on the reference signal, which cancels any drift effect.

For each channel, data is recorded at a total of 154 angle positions per revolution of the scanner optics. The data is further processed by software to compensate for differences in offset or gain for each of the 32 detectors. The power is then calculated from the corrected I/Q components, combined with the position information from the angular encoder of the driving motor, and used for the generation and on-screen display of a real-time or close-to-real-time image.

This is achieved by a triangulation technique which averages and interpolates the data. The software spans a triangular net over the field of view consolidating the measured $154 \times 32$ data points into approximately 2000 effective pixels. Considering the diffraction-limited spot size, we oversample the field of view slightly by a factor of about 2.6 ($2000 \cdot \pi \cdot (0.75\ \text{cm}/2)^2/13 \times 26\ \text{cm}^2$), which is desirable.

Fig. 5 shows a reflection image of the handgun of Fig. 1. At the present time, the performance of the system is still limited by three aspects. First, the targeted power level of the source of $\geq$1 mW could not yet be reached, but so far has been limited to $\leq 105\ \mu$W. Second, the manual assembly of the detector blocks led to significant variations in detector sensitivity by up to 20 dB, which could be compensated only partially by data processing in the software. And finally, we found that a lower IF, further away from mobile phone frequencies, strongly reduces crosstalk between channels and pick-up of external signals. After implementation of corrective measures, the system will be ready for field tests.

To summarize, with this portable and fully electronic system, real-time standoff imaging at 812 GHz has been successfully demonstrated for the first time. A maximum frame rate of 12 fps and a spatial resolution of 7.5 mm at 4 m distance has been achieved. With a sufficiently homogeneous detector performance, the identification of security-relevant objects, e.g., a handgun (Fig. 5), is possible. The system described here is conceptually quite similar to the 620-GHz single-pixel imaging radar system of [12]. With that second-generation machine, the authors have demonstrated the principle capability to detect objects such as pipe bombs concealed under clothes, with 0.5 mW of power for illumination at a distance of 25 m. There is no reason why our system, after optimization, should not perform in a similar way, but in real time and not with the 5-s data acquisition time dictated by the single-pixel operation of the system of [12].

We now come back to the FMCW imaging approach. Frequency modulation of the THz wave allows time-of-flight ranging. When the frequency sweeps are performed with a high repetition rate, FMCW ranging can be readily combined with scanning imaging as described before. Three-dimensional (3-D) imaging significantly improves object identification [12], which otherwise represents a major challenge for THz imaging modalities.

With the FMCW method, the range of uniqueness for the determination of the distance is much larger than with single-frequency phase measurements, but the depth resolution is lower: When we denote $c$ as the speed of light, and $\Delta\nu$ as the chirp bandwidth, the fundamental limit for the depth resolution is given by $c/(2\cdot\Delta\nu)$. Applications like standoff imaging can benefit from FMCW because the ranging resolution and range of uniqueness fit much better to their demands than the high-resolution, half-wavelength range of uniqueness provided by phase measurements.

Fig. 6 provides a demonstration, how the range information provided by FMCW imaging can facilitate the recognition of an object. The example shown in this figure is a raster scan with a SynView300 transceiver working around 300 GHz with a chirp wavelength of 90 GHz (230–320 GHz) and a FMCW sweep time of 240 $\mu$s. In the power reflection data of the top panel of Fig. 6, one can recognize the hand, but only because the contour of the hand is clearly identified by the signal reflected from the metallic background on which the hand rests. The hand in free space would only provide strong signals from those parts of it which reflect specularly. An object recognition will, in general, be difficult. This is different with the time-of-flight data. Here (see bottom panel of Fig. 6), the hand is clearly identified.

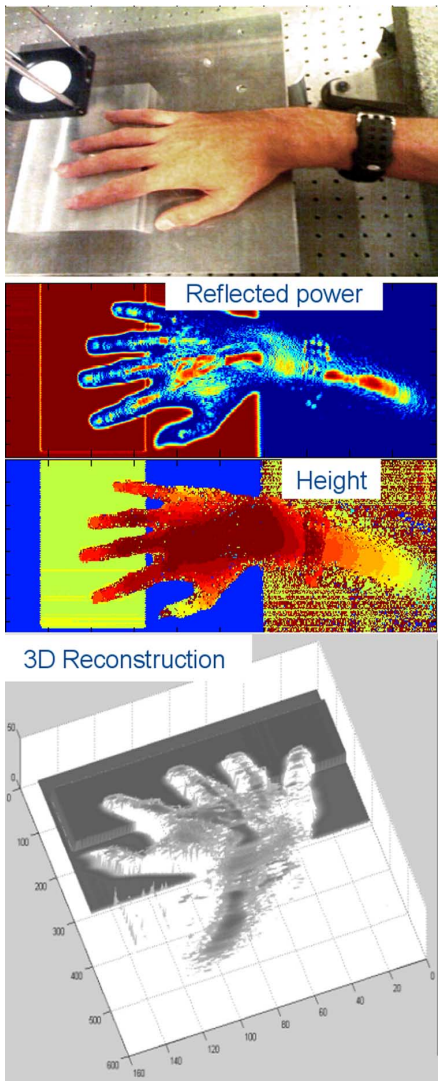


Fig. 6. 300-GHz raster-scan images of Torsten Löffler's hand. The photograph shows the experimental situation in the visible range: The hand rests on metal blocks below the white teflon lens of the THz imaging system (the illumination and detection beam paths are equal). Second panel: reflected power image; third panel: time-of-flight data representing the height profile; bottom panel: 3-D reconstruction of the hand employing the THz data. While one can only recognize certain features in the reflected power image (if the reclection of the metallic background on which the hand rests is disregarded), the 3-D reconstruction gives a much clearer impression of the object.

### *B. Synthetic-Aperture Imaging*

We now address the synthetic-aperture approach of imaging. Here, a number of sources (transmitters, Tx) and detectors (receivers, Rx) are arranged either in a line or in a two-dimensional (2-D) configuration. The transmitters illuminate the scene, while the receivers collect the scattered energy. The coherent signals from each Rx/Tx combination are acquired and numerically transformed to the image data for the corresponding line in the object plane [25]. Multi-element arrays have been demonstrated predominantly at millimeter-wave frequencies [26]–[29] while most higher frequency synthetic-aperture systems have been using a scanning of a single element and synthetic-aperture reconstruction.

The advantage of synthetic-aperture over conventional imaging is the need for fewer or no moving mechanical parts. This can enhance data acquisition speeds tremendously, but comes at the price, that more electronic components are needed and that the numerical effort of image reconstruction is enormous. An additional advantage of synthetic-aperture imaging is that there does not exist a focal plane as in conventional systems. The object can principally be imaged with equal resolution over a considerable range of depth.

Synthetic-aperture techniques with minimum redundancy in 2-D arrangement have been successfully presented in [30], but only for passive systems. Active imaging system configurations with low redundancy are only known for line configurations [31].

The THz camera considered here has been designed for operation at standoff distances of $\geq$8 m, with a scene area of $0.7\times 2\ \mathrm{m}^2$ and producing images close to real time. Quasi-optics is employed for one dimension only (vertical direction, focusing of the scanned line) and hence consist of cylindrically shaped mirrors. The other dimension (imaging of the line) is handled by synthetic reconstruction.

The angular resolution, $\alpha$, is determined by the overall size of the linear antenna array $N_{\mathrm{Tx}} \cdot N_{\mathrm{Rx}} \cdot \Delta_{\mathrm{Rx}}$, where $\Delta_{\mathrm{Rx}}$ is the Rx antenna element spacing:

$$\alpha = \frac{\lambda}{N_{\mathrm{Tx}} \cdot N_{\mathrm{Rx}} \cdot \Delta_{\mathrm{Rx}}}. \tag{1}$$

With a wavelength of $\lambda = 1$ mm, this results in $\alpha = 0.0015625$, for 8 Tx and 16 Rx elements, and an Rx element spacing of $\Delta_{\mathrm{Rx}} = 5$ mm. At a distance of 10 m, the spatial resolution is then $\Delta_S = 15.6$ mm. The angular ambiguity separation is $\theta = N_{\mathrm{Tx}} \cdot N_{\mathrm{Rx}} \cdot \alpha = 0.2$. This assumes that no redundancy in the Tx and Rx elements has been introduced according to algorithms presented in [31]. The realized components have, however, finite dimensions and cannot be positioned at the exact locations, which in turn deteriorates the spatial resolution to $\Delta_S \approx 20$ mm.

A large time-bandwidth product of the transmitted signal is necessary in order to obtain good signal-to-noise performance (requiring long pulses) simultaneously with good range resolution (requiring large bandwidth). The temporal range window $\tau_f$ should be chosen shorter than the uncompressed pulse length $\tau_p$ in order to simplify the baseband system. The minimum pulse length, which must be recorded to focus the range window, is $\tau_r = \tau_p + \tau_f$. For a scene with a range extension of $\Delta r$, the required IF bandwidth $B_{\mathrm{IF}}$ (and ADC bandwidth) after analog deramp is a fraction of the modulation bandwidth $B_p$

$$B_{\mathrm{IF}} \geq N_{\mathrm{Tx}} \cdot \Delta f_{\mathrm{Tx}} \geq N_{\mathrm{Tx}} \cdot \frac{\tau_f}{\tau_p} \cdot B_p. \tag{2}$$

The ambiguous range is determined by the transmitter frequency separation $\Delta f_{\mathrm{Tx}}$ between individual channels:

$$r_{\mathrm{amb}} = \frac{c \cdot \Delta f_{\mathrm{Tx}} \cdot \tau_p}{2 \cdot B_p}. \tag{3}$$

The image acquisition and processing of a line is performed with a refresh rate of $\tau_r < 5$ ms, for an operating frequency regime of 220–320 GHz with a modulation bandwidth $B_p = 100$ GHz. For an uncompressed pulse length $\tau_p = 1$ ms and a Tx frequency separation $\Delta f_{\mathrm{Tx}} = 1$ MHz, the ambiguous range is

Fig. 7. CAD representation of the scanning synthetic-aperture imaging system. The line of emitters and detectors is visible on the top left side of the system (brass-colored components). The scanner has the dimensions: 1 m × 2 m × 1.5 m. The dimensions of both large mirrors are 1 m × 0.7 m. The mirror is designed to rotate with 0.5 Hz. The radiation from the emitters hit the narrow cylindrical reflector located under them, which steers the beams to the large fixed mirror at the top right edge. From here, they impinge onto the rotating triangular deflector which illuminates the scene at the right side of the system. Reflected radiation returns along the same path in the opposite direction.

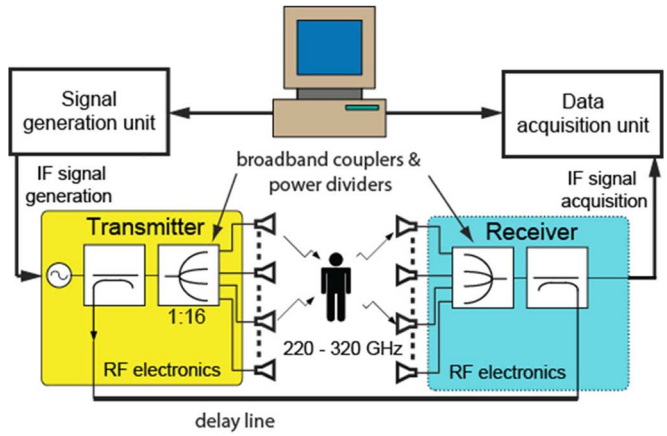


Fig. 8. Block diagram of the electronic imaging system.

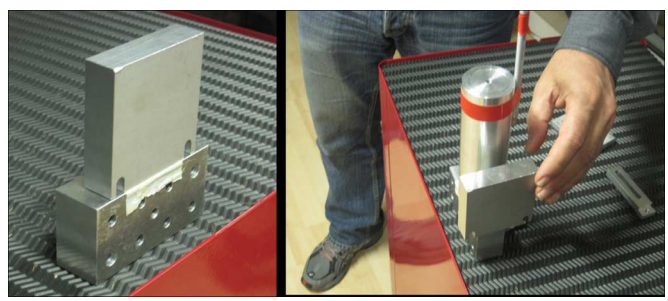

Fig. 9. Measured targets employed for the verification of the synthetic aperture imaging system.

$r_{\mathrm{amb}} = 1.5$ m. For every pulse and for every pixel in the output image, an interpolated sample must be computed and accumulated. Fast back-projection algorithms exist [32]–[34], including near-field scenarios, with improvements in speed by a factor of 100 compared with direct back-projection in 2-D [33], [34]. These algorithms have the advantage of providing the flexibility and robustness of a time-domain algorithm but exhibiting a computational performance in parity with fast transformation algorithms.

The mechanical layout of the imager is illustrated in Fig. 7. The system combines a linear array of emitter–receiver elements, used for synthetic imaging in the horizontal direction, with classical scanning optics for the vertical direction, the latter employed in order to keep the numerical effort of image reconstruction limited for the sake of the real-time capability of the system. Currently, the system employs 16 Rx units and 8 Tx units with 8-mm receiver and 128-mm transmitter spacing. The eight transmitters are switched sequentially and each of them provides an output power of approximately 1 mW. The beam divergence is determined by the horn antenna of each emitter unit.

Fig. 8 displays schematically the operational concept of the system. The distribution network is prepared for 16 Tx units, but only 8 were employed at the experiments. The FMCW approach provides the depth resolution, while the emitter-detector line array generates the data for synthetic image reconstruction. The data acquisition system, which copes with the high data stream, is built around SPECTRUM ADC and DAC cards and a Cyclone Microsystems backbone. The delay line connecting the transmitter and the receiver is a fixed delay line employing a 50-Ω semi-rigid coaxial cable.

Real-time reconstruction was demonstrated using a parallel implementation of the back-projection algorithm on an NVIDIA GTX260 graphics processing unit (GPU). A $1 \times 1$ m$^2$ $x$–$y$-slice of $128 \times 128$ pixels could be focused in less than 2 ms.

Concurrent operation of all Tx and Rx modules could not be achieved here, due to errors in the I/Q modulators employed in the current design. This will become available in a redesigned version of the system. The system has been tested with objects close to the spatial resolution limit of the system with a fixed position of the rotational triangular mirror.

Fig. 9 illustrates a few of the test objects at 8 m distance from the scanner, and measured with 200 averages, leading to a measurement time of about 200 ms. The objects are an aluminum block with 7.5 × 7.5 cm size (left side of Fig. 9), and a metal block with a 2.5-cm-wide illuminated front side and a cylindrical aluminum post with a radius of 2.5 cm, respectively (right side of Fig. 9).

Results of measurements are shown in Fig. 10(a)–(d) for the objects of Fig. 9. The distance reading (around 7 m) is referenced to the mounting rack and not to the emitter/detector units (total distance with respect to these: about 10 m). The top panel shows the signature of the large aluminum block. A close-up look at the result at 0-dB level reveals a sharp line at 7.01 m with 7.5-cm width. This is in very good agreement with the object. However, there is a significant spill-over towards negative cross-range values. The source of this spill-over has not been identified unambiguously yet, possible causes being i) a slight misalignment of the optics, to which the reconstruction algorithm is quite sensitive, or ii) thermal fluctuations in one of the

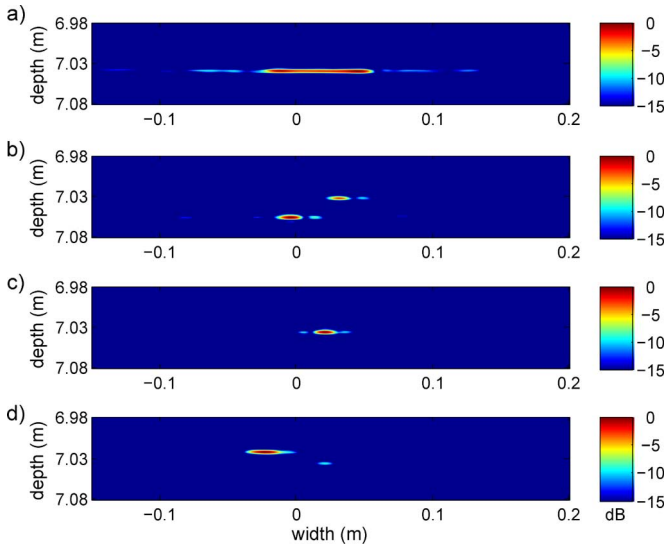


Fig. 10. Synthetically reconstructed images of objects presented in Fig. 9: a) a 7.5-cm-wide metal block, b) two 2.5-cm-wide metal blocks separated by 7.5 cm, c) a cylindrical metal post with a radius of 2.5 cm, and d) the cylindrical metal post together with a 2.5-cm-wide metal block. Numbers on the axes are in units of meters.

eight Rx blocks of the array. In addition, one can observe sidelobes in the figure. The sidelobes in all results are below 3 dB but cannot easily be explained with parasitic reflections. We have therefore performed point target simulations with different receiver numbers and separations of the Rx and Tx elements. The simulations suggest that a part of the receiving elements were not fully operational, and that the Rx spacing differs from the envisaged 8 mm. The predicted sidelobe levels for the nominal spacing should be below -20 dB.

Fig. 10(b) shows the results for two aluminum blocks whose width of 2.5 cm is close to the resolution limit. The objects should then act essentially as point-like scatterers. The object separation is clearly resolved and the objects indeed have signatures close to those of point-like targets. Fig. 10(c) shows the reconstructed image of the cylindrical pillar. The dimensions of the pillar and its range position are well reconstructed, with values around 2.5 cm and 7 m, respectively. The pillar should appear as a point-like target, which is nicely the case in the reconstruction.

We have finally positioned the cylindrical pillar in direct contact with the narrow block, as indicated in Fig. 9. The corresponding data in Fig. 10(d) reveal that the pillar provides the strongest signal and the block contributes to the signal on the right-hand side of the pillar.

In summary, a first proof-of-principle demonstration for synthetic-aperture imaging in the 300-GHz frequency regime has now been provided. The system does not yet operate in real-time, but should be capable to do so in the future; the system is being improved further for more detailed studies.

### *C. Summary and Potential of Active Electronic THz Imaging Systems*

All-electronic real-time imaging has progressed rapidly due to advancement in semiconductor technology and improvements in system architecture and image reconstruction algorithms. As promising as it is, there are still major constraints to be overcome. The available output power from a single source is very limited beyond microwave frequencies, which limits the overall dynamic range. Low-noise amplification has seen tremendous progress, while output power improvement has advanced on a much slower pace. Comparing with the power level of kilowatts readily available in the microwave regime, it is amazing what has been achieved with the mWs of power and less, available to us at acceptable costs in the THz regime. This situation limits the current dynamic range of multi-element imaging radar systems to 40–70 dB, in contrast to $\geq$ 100-dB dynamic range at lower frequencies. Multi-static concurrently measuring imaging radars are important for real-time operation, but their architecture is still a subject of intensive research, especially with regards to calibration issues.

Dramatic improvements have been observed in the area of image reconstruction algorithms. These have profited from the introduction of novel SAR (synthetic-aperture radar) systems at lower frequencies and from the work performed on 77-GHz systems for automotive industries. Several real-time algorithms have been proposed and implemented on GPU computer workstations. The bottleneck here is the data acquisition hardware, which has to sustain the very high data flow of gigabytes per second. With appropriate data reduction algorithms it is believed to be possible to reduce the data stream and to implement the algorithms on more convenient machines.

## III. Optoelectronic Terahertz Imaging Systems

Here, we describe the development of THz imaging systems employing multi-pixel EO detection, where the THz image information is transferred to the visible/near-infrared spectral range via EO mixing and subsequently measured using a commercial optical camera (e.g., CCD/CMOS). This allows one to project the complexity of multi-pixel detection onto a highly developed technology, albeit at the price of a limited EO conversion efficiency and hence a reduction in the dynamic range. EO detection provides a measure of the field amplitude and phase (similar to heterodyne electronic detection) but can also be extended to THz frequencies well above 1 THz.

In this context, the emphasis of our work has been placed on the realization of both a homodyne and a heterodyne THz imaging system. The homodyne approach takes advantage of a nanosecond pulsed quasi-CW THz OPO in combination with a CCD camera for homodyne EO readout, while the heterodyne approach is based on a hybrid system with a quartz-stabilized CW microelectronic THz emitter in conjunction with an EO demodulating camera detector.

Here we describe each system in turn, including THz beam image measurements, a comparison of their relative current performance, and directions for further improvement of each system.

### *A. The Homodyne Concept*

The homodyne approach has been guided by the elegant way of multi-pixel THz imaging introduced by the group of Zhang in conjunction with THz pulses generated by a femtosecond amplifier laser system [35]. Recently, this approach has allowed real-time imaging using a 1-kHz repetition rate laser and a state-of-

the-art CMOS camera [36]. However, for practical applications, amplifier laser systems are typically too expensive and are difficult to deploy and maintain outside a laboratory environment. Multi-pixel EO THz imaging was also pursued with an optoelectronic CW source [37], although it was found that the THz power was too low for effective imaging; averaging over 40 min was required to measure the spatial profile of the focused THz beam.

Hence as a compromise between femtosecond- and CW-systems, we decided to explore the use of a THz OPO pumped by a 10-kHz $Q$-switched Nd:$YVO_4$ laser at 1.06 $\mu$m. Such THz-OPOs emit quasi-CW THz radiation, with the emission in bursts with typical pulse duration of $\sim$10 ns, at a repetition rate from anywhere between 10 Hz–10 kHz [38], [39]. For instance, at a low repetition rate of 15 Hz, very high peak powers of $>$1 W can be generated [39], which translates into a peak field of $>$150 V/cm (assuming moderate focusing to a 1-mm beam radius). For the higher repetition rate of 10 kHz, such as the THz-OPO used here, peak powers of several 10 mW can still be readily achieved, corresponding to peak fields of several 10 V/cm (again assuming a beam radius of 1 mm).

Such THz-OPOs can reach considerably higher THz field amplitudes than typical truly-CW emitters, such as a multiplier-chain-based electronic source—with our 0.65-THz emitter, we obtain a power of $\sim$1 mW, which translates into a field amplitude of 5 V/cm. To put this value further into perspective, we note that a high-repetition-rate fs Ti:sapphire laser can generate THz pulses with an average power of 40 $\mu W$ [40], [41] corresponding to a peak power of about 400 mW which, when focused, provides a field amplitude of the order of 100 V/cm. This is much less, though, than what can be achieved with amplifier-based Ti:sapphire sources, which achieve tens to one hundred kV/cm with semiconductor-based THz emitters [42], and even reach higher with laser-induced plasmas [43], [44].

If one estimates with the peak fields of our THz-OPO and the known parameters of EO detection, over how large an area of an object one may be able to take diffraction-limited images with a camera, one finds that 100-pixel parallel detection should be possible in real-time mode for reflective imaging[1] [45]. While a limited parallelism alone will not yield detailed pictures per se, one can imagine a parallel imaging modality involving an additional scanning of the object, e.g., via a line scanner.

In the following, we experimentally explore multi-pixel detection with our THz-OPO and a Si CCD camera. The experimental setup is displayed in Fig. 11 [46]. Quasi-CW THz radiation bursts are generated at a repetition rate of 10 kHz directly in a periodically poled $LiNbO_3$ crystal in the OPO cavity together with the signal wave [47]. Seeding at the signal wavelength enhances the conversion efficiency. The difference frequency of the pump and signal waves is equal to the frequency of the THz radiation. A key advantage of this OPO is that the two near-infrared beams, whose superposition is required for the EO detection, exit the OPO collinearly. After cleaning of the beam modes in an optical fiber, the dual-color beam is available for EO detection of the THz radiation, which is coupled out from the $LiNbO_3$ crystal via a set of silicon prisms, and overlaid with the readout beam with the help of an indium-tin-oxide dichroic beam combiner [48]. The frequency of the THz radiation of 1.5 THz is fixed by the poling of the crystal. We have chosen a 1-mm-thick CdTe (110) crystal as a suitable EO detection crystal for this optical wavelength and THz frequency [49]. The peak power of the THz radiation was found to be 13 mW directly behind the Si prism coupler [46]. For a focal spot with a radius of 1 mm, the corresponding field strength is $\sim$18 V/cm.

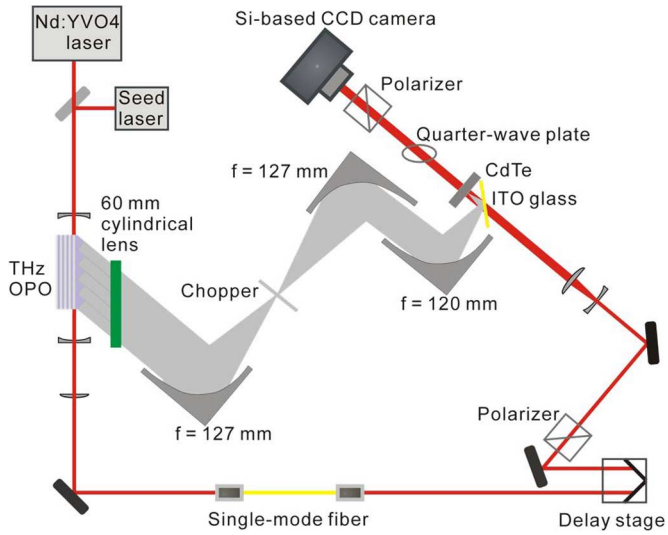


Fig. 11. Schematic of the THz imaging system based on a ns quasi-CW THz-OPO with multi-pixel cross-polarizer EO detection.

We first performed single-pixel raster-scan imaging with EO detection in a crossed-polarizer geometry and Ge photodetectors. The THz beam profile was measured without a sample in the beam. The near-infrared dual-color readout beam was tightly focused and raster-scanned across the EO crystal.

These measurements yielded a dynamic range of 28.3 dB/Hz and a NEP of 1.87 nW/Hz at the peak of the focal spot. Note that the values in [46] are revised here to correctly account for the effective detection bandwidth $B_{\rm eff} = 1/(6\tau)$ (filter slope of 12 dB/oct) where $\tau = 50$ ms is the lock-in time constant, and we now use the correct units for coherent detection, i.e., dB/Hz instead of dB/$\sqrt{\rm Hz}$). The dynamic range is calculated from the ratio of the maximum EO lock-in signal $(S)$ to the rms noise level in the absence of the THz beam $(\sigma)$ via $\mathrm{DR} = 20\log_{10}(\sqrt{B_{\rm eff}}S/\sigma)$, while the NEP is obtained from $\mathrm{NEP} = B_{\rm eff}(\sigma/S)^2P$ (where $P = 1.3$ $\mu$W is the average THz power). While these single-pixel measurements employed differential detection with a reference Ge detector, the limiting noise source is still due to residual laser fluctuations (i.e., not shot-noise limited) due to a small loss in the common mode fluctuations induced by the optics in the EO detection arm.

[1]To reach such a result, we consider a system with an input average THz power of $\bar{P} = 4$ $\mu$W, corresponding to a peak power of $P_0 = 40$ mW. Assuming a power collection efficiency of $10^4$ from the scattering object, we have a THz peak power of $P = 4$ $\mu$W at the EO detector, which translates to an electric field amplitude of $E = 6$ Vm$^{-1}$ in the EO detection (assuming 100 effective pixels, each an area of $(3\lambda)^2$ at 1 THz). Based on the typical sensitivity of crossed-polarizer EO detection [35] (modulation depth coefficient $k_{\rm EO} = 2.5\times10^{-6}(\mathrm{Vm}^{-1})^{-1}$), the achievable modulation depth is $1.5\times10^{-5}$. This is equal to the relative shot noise of a CCD/CMOS camera system (such as the CCD employed here, described below) after binning from $10^6$ CCD pixels down to a hundred THz-image pixels with a 50-ms integration time.

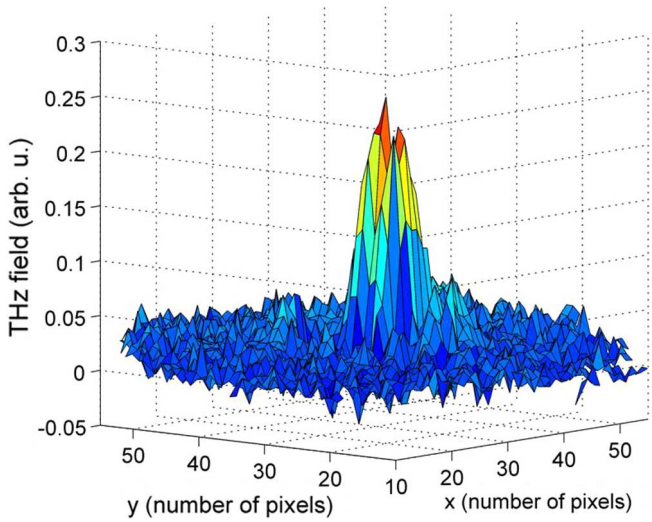


Fig. 12. CCD-recorded EO field image of the focused THz beam from a THz-OPO. The $x$–$y$ scaling represents binned camera pixels resulting in an effective pixel size in the focus of $192 \times 192$ $\mu$m$^2$.

The diameter of a diffraction-limited Airy disk on the EO detector is about 0.7 mm under the given experimental conditions. With a diameter of the THz beam of 2 mm, the number of effective optical pixels covered is about 10. Hence, for a pixel number of 100 (i.e., with a $\sim$3 times larger spot diameter) the achievable dynamic range would then be reduced to 18.3 dB/Hz.

We now come to parallel camera-based imaging. The Ge detector was replaced by a Si CCD camera (Dalsa 1M60CL) having $1024 \times 1024$ pixels, a large full-well capacity (FWC, $1.5 \times 10^5$ electrons), and a 12-bit low-noise readout. The optical beam was expanded to cover an area of about 1 cm$^2$. The camera acquires 50 frames/s (with fast CPU processing of the 150-MB/s frame data), and the THz beam is mechanically chopped at 25 Hz, allowing one to extract a differential THz field image by subtracting bright and dark frames.

Fig. 12 shows a measured field-amplitude profile of the THz beam for a fixed position of the delay stage (fixed relative phase between THz wave and amplitude modulation of optical beam), using an integration time of 120 s (i.e., 3000 light/dark frames), where we apply $16 \times 16$ digital binning to yield a $64 \times 64$-pixel image. The relative modulation depth of the peak signal was $3.5 \times 10^{-4}$, which is close to that expected from the field strength in the EO crystal predicted from the power measurements, taking into account THz losses, the crossed-polarizer geometry and the imperfect temporal overlap of the dual-color pulses [46]. Based on the noise floor (from a reference measurement without the THz beam) the dynamic range relative to the peak signal is 17 dB. Taking into account the effective measurement time of 120 s, the integration-time-corrected value is then $-3.8$ dB/Hz. However, very recent measurements with a higher THz field have achieved a relative modulation depth of $1.2 \times 10^{-3}$ and a dynamic range of $+9$ dB/Hz [45].

Nevertheless, this performance is considerably lower than that of single-pixel measurements. This is attributed to signal fluctuations both from the laser (which in this case, are not normalized at all by a reference detector) and the asynchronous frame acquisition/chopping, both of which lead to a relative noise of $> 10^{-4}$ for a 1-s integration time.

Hence, two clear directions for improvement of the current system would be to add a reference detector to normalize each acquired frame (although here care must be taken to correctly account for the detection of the two wavelength components of the dual-color optical beam, which are not correlated due to the fact that the signal beam depletes the pump beam in the OPO), and to trigger the camera synchronously to a subharmonic of the pulse train.

If these noise sources can be sufficiently well suppressed, one can approach the significantly lower detection limit due to shot noise (which exceeds the readout noise here). Given the current pixel FWC and assuming binning to a $64 \times 64$-pixel image, this sets a relative noise level of $4.6 \times 10^{-5}$ for the differential THz image with a 1-s integration time (i.e., over an order of magnitude smaller than the modulation depth) which would result in a dynamic range of $\sim$28 dB/Hz.

In principle, it is possible to improve the performance of this ns-THz-OPO system even further. Firstly, the EO modulation depth could be improved by either increasing the THz power, or by improving the EO mixing by using a crystal with a larger nonlinear coefficient or coherence length. Moreover, as the THz radiation here is quasi-CW, narrowband quasi-phase matching schemes are also applicable (in contrast to broadband pulsed THz systems). Secondly, the use of emerging state-of-the-art CCD/CMOS with a larger photo-electron throughput (FWC $\times$ pixel number $\times$ frame rate) would allow the shot noise level to be further reduced. Without such improvements in the throughput, it is also not possible to exploit the far higher detection quantum efficiency of InGaAs-based cameras at this $\sim$ 1-$\mu$m wavelength, as one simply reaches the pixel saturation at a lower incident optical power.

### *B. The Heterodyne Concept*

Our novel heterodyne EO imaging concept is based on a hybrid setup, in which the incident radiation of a quartz-stabilized CW THz source is electrooptically mixed [50] with either a femtosecond-laser [8], [51], [52] or a synchronized CW diode-laser pair [53], whose EO modulation is captured with a photonic-mixing device camera (PMDtec PMD[vision] 3k-S [54]) [55], [56]. Such PMD cameras were originally developed for 3-D time-of-flight imaging with near-infrared radiation [57], [58], and allow phase sensitive detection of a modulated optical signal. As the repetition rate of the optical pulses/intensity modulation is incommensurate with the CW THz frequency, the EO signal is modulated at an intermediate frequency (in our case, 10 MHz), with a modulation phase dependent on the phase of the THz wave. This EO signal is then demodulated by the PMD camera, allowing one to recover both the THz amplitude and phase. The camera used here has a $64 \times 48$-pixel sensor with 0.1-mm pitch.

As shown in Fig. 13, each pixel consists of two transparent photo-gates between two readout diodes, which are connected to the readout circuitry. A push-pull modulation of the photo-gates controls the charge carrier transport to the readout diodes and hence acts like a charge swing. As the small EO signal modulation is synchronized with the pixel modulation frequency,

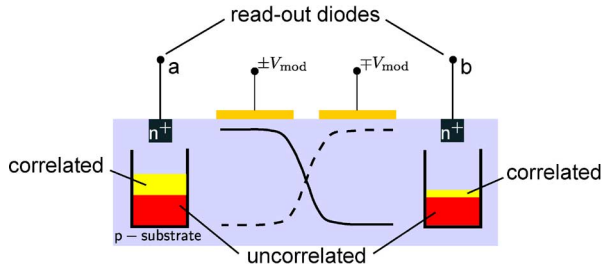


Fig. 13. Schematic of a single PMD pixel.

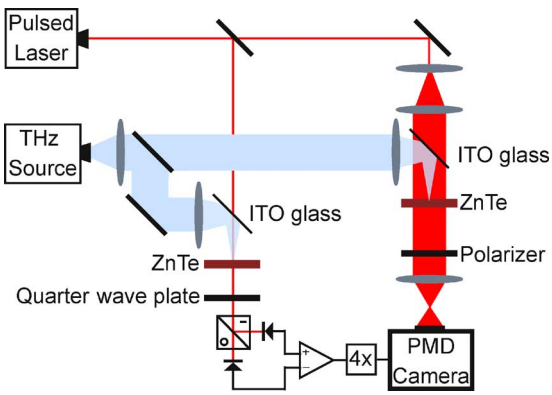


Fig. 14. Scheme of the heterodyne hybrid EO THz imaging system, employing an electronic THz source, fs optical pulse train for detection, and a PMD camera for demodulation of the EO signal.

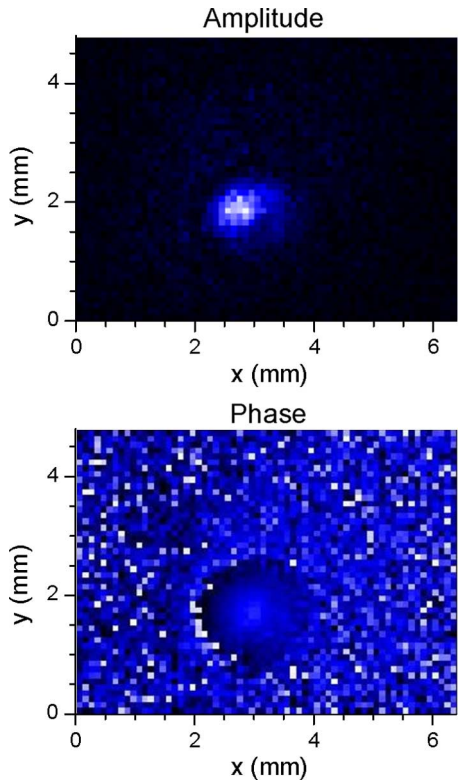


Fig. 15. EO image of the THz field amplitude and phase for a focused beam with the heterodyne hybrid system of Fig. 14, using an image reduction factor of 2 (data taken from [56]). The size of the image is 6.4 mm × 4.8 mm. The radius of the spot of well-defined phase is 0.8 mm; the corresponding radius on the crystal is 1.6 mm.

one measures a charge difference between the two output channels proportional to the EO signal (and hence, THz field amplitude) depending sinusoidally on the phase shift between these two modulations (whereas the constant background light creates equal output signal components which cancel). Consequently, the phase information of the detected signal can be retrieved by several suitable measurements with equidistant phase shifts of the pixel modulation. To extend the dynamic range of acceptable unmodulated background, a circuit for the suppression of background illumination (SBI) is integrated in every pixel. This circuit drains integration capacitors equally from charge carriers resulting from uncorrelated background [57].

The scheme in Fig. 14 illustrates the implementation of the PMD-camera into the hybrid setup using a femtosecond-laser system for the EO imaging of a THz focal spot. Both a reference and an imaging branch are provided with an equal portion of the radiation from a quartz-stabilized microelectronic 0.65-THz emitter (Radiometer Physics GmbH) with 1.1-mW output power. Each branch contains an EO detection unit, which uses the pulses from a high-repetition-rate femtosecond Ti:Sapphire laser system (Spectra Physics, Tsunami) as the optical probe light. Indium–tin–oxide dichroic beamsplitters [48] are used to combine the THz and optical beams, which then propagate collinearly to the EO crystal ($\langle 110 \rangle$-oriented ZnTe).

The THz field is electrooptically mixed with the optical pulse train, which acts as the LO signal in this heterodyne setup, producing an optical modulation whose lowest frequency component lies at an intermediate frequency of ∼10 MHz (due to mixing of the 0.65-THz wave with the ∼8100th harmonic of the repetition rate of the optical pulse train). This IF can be tuned by adjusting the length of the laser cavity, and hence the pulse repetition rate. Due to the inherent stability of the femtosecond laser, no active synchronization scheme is required.

The reference branch is based on a (single-pixel) balanced EO scheme with a focused optical beam [59], and is used to provide a strong reference signal at the IF, which is required for the external pixel modulation input of the PMD camera. Due to the design of the PMD hardware, we must generate the fourth harmonic of the reference signal for this input, as this is used internally to generate four 90°-shifted reference signals at the IF, as is needed to retrieve the EO signal amplitude and phase.

The readout unit of the imaging branch comprises a large-area 1-mm-thick ZnTe crystal in a crossed-polarizer setup [60] with an expanded optical beam (average intensity 200 mW/cm$^2$). For these measurements, the incident THz radiation is focused into the EO crystal, where we estimate a field amplitude of ∼1.5 V/cm based on the measured focal beam radius of ∼1.4 mm. The EO crystal is imaged with a reduction factor of 2 onto the sensor of the PMD camera.

The image of the THz focal spot in Fig. 15 was effectively recorded within 2.5 s and shows a dynamic range of 23 dB/Hz. The measurements were taken close to the saturation limit of the PMD camera, which resulted in the best possible SNR. However, the measurements suffer from slight inhomogeneities of the pixels, obstructing the detection of the weak EO signal by a considerable background signal, which varies from pixel to pixel. This necessitated the additional measurement of dark

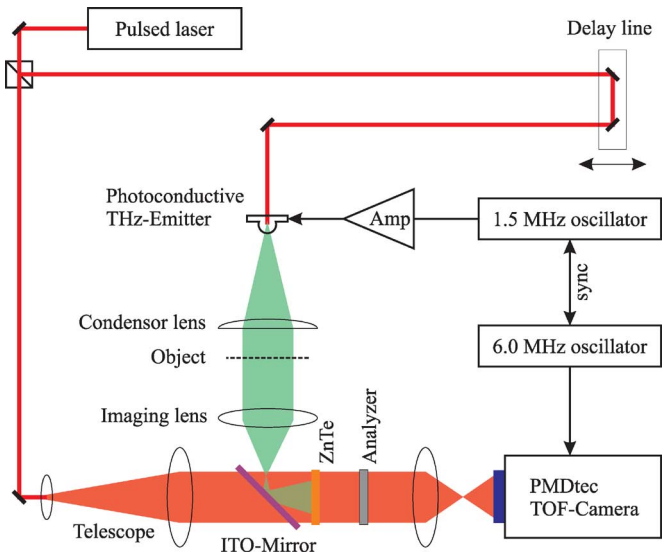


Fig. 16. Scheme of the THz-pulse EO imaging system comprising a modulated photoconductive THz-pulse emitter and a PMD camera for the demodulation of the EO signal. The NIR-converter of Fig. 14 is utilized; it is depicted here in more detail. In this system, the laser beam is split, one portion driving the photoconductive emitter, the other serving for EO sampling. The relative timing of the THz pulses and the optical pulses can be adjusted via the delay line. This allows imaging with high temporal resolution for the monitoring of the THz-pulse evolution, e.g., for the extraction of spectral information (not exploited here).

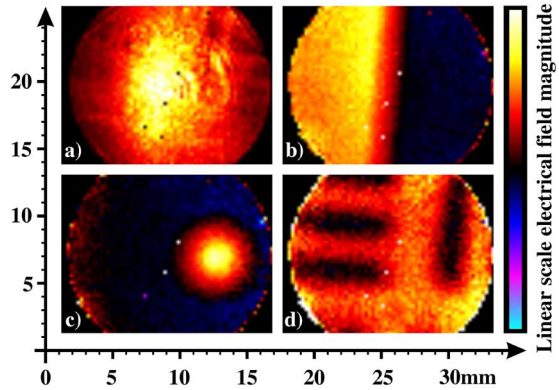


Fig. 17. THz images recorded with the THz-pulse imager comprising the PMD camera: a) Beam profile; b) edge of a steel sheet; c) 4-mm-diameter aperture; and d) part of element −2.2 of an USAF resolution target. Images b)–d) have been normalized to beam profile to enhance weakly illuminated regions.

frames (i.e., with the THz beam blocked), subsequent to THz image recording, to allow subtraction of this spatially noisy background. Hence, the 2.5-s effective integration time of the THz images comprises both 2500 bright and 2500 dark frames, each with a frame integration time of 0.5 ms. Due to the restricted pixel capacitance, longer integration times were not possible. The limited speed of the camera's embedded computer for data preprocessing and IEEE-1394-Firewire communication extends the total data acquisition time of the image to several minutes.

Although the present system possesses these drawbacks, it is important to note that the current commercial PMD cameras are designed for time-of-flight measurements of directly modulated near-infrared radiation, and thereby are not optimized for the small EO modulation depth. The development of PMD cameras with larger pixel capacitance and more homogeneous readout channels in the detector array could significantly improve the performance of the heterodyne EO THz imaging system presented here.

In order to take advantage of the higher electric fields of THz pulses, we also implemented a THz-pulse-based imaging system in which the EO signal is demodulated by means of a PMD camera [55]. The setup, which is displayed in Fig. 16, is again a THz-illumination/optical-probing arrangement, but now the optical pulses are used for both the generation of the (pulsed) THz radiation and for the EO readout.

Femtosecond laser pulses from a high-repetition-rate Ti:sapphire laser (Coherent Mira 900) generate THz pulses in a photoconductive antenna whose bias voltage—and with it the amplitude of the THz pulse train—is modulated. The average power of the THz radiation was determined to be $\sim 2\ \mu$W. With the THz beam, we perform transmission measurements. The THz signal is then read out in an EO crystal, where the information of the image and the modulation of the THz beam are transferred onto the optical readout beam. There is no need for a reference detector, because the modulation signal of the emitter is fed into the PMD camera synchronously with the reference signal which allows to use the full available THz power for the imaging path.

In contrast to the heterodyne setup using the hybrid system described above, here, the THz beam is collimated and not focused, allowing imaging of small objects. Fig. 17 shows examples of THz images. Frame a) depicts the beam profile whose amplitude distribution was then used to normalize the other THz images in order to enhance weakly illuminated areas at the boundary regions of the field of view. The following frames show b) an edge of a steel sheet, c) an aperture with a diameter of 4 mm, and d) element −2.2 of an USAF resolution target. The images altogether indicate that the lateral resolution is in the order of 2–3 mm. The image data were recorded with an effective integration time of 8, 2.5, 0.6, and 2.0, respectively. Owing to the comparatively high peak field of the femtosecond pulses from the Ti:sapphire, this imaging setup yields a dynamic range of 44 dB/Hz. These results demonstrate that the PMD-based EO-imaging system performance improves rapidly with higher THz fields (i.e., EO modulation depths), and is already an attractive option for a range of fs-optoelectronic-based THz imaging applications.

### *C. Summary and Potential of Optoelectronic THz Imaging Systems*

In comparing the two (quasi)-CW EO THz imaging systems presented in the previous sections (Sections III-A and III-B), despite certain issues for each system, the current performance of the heterodyne system (dynamic range 23 dB/Hz) is significantly higher than that of the homodyne system (9 dB/Hz). Indeed, this could be expected to be the case, as the CW-hybrid heterodyne system with a PMD camera can exploit the far better noise rejection at the 10 MHz detection frequency (which is above the noise bandwidth of many laser systems).

We note, however, that for both systems the multi-pixel performance is degraded significantly compared to that of the corresponding single-pixel detection—i.e., with single PIN photodiodes and a lock-in amplifier (with the same detection frequency)—even though our imaging measurements here were made with focused THz beams. As described above for each system, this indicates that the key direction for improvement at present is on the implementation of the optical camera detection (CCD, PMD), in order to approach the shot-noise detection limit where a far higher dynamic range can be expected. For applications where a reduced pixel number would be acceptable, an interesting alternative is to use PIN photodiode arrays (e.g., a line array with $\sim$50 detectors) [14], although for the heterodyne system this would require large-scale multi-channel lock-in amplifier electronics, which are already integrated elegantly and inexpensively in the PMD camera design.

Based on our existing results, the dynamic range of the PMD-based EO-imaging system is significantly improved when using a fs-laser-pumped THz emitter, due to the high peak fields of the THz pulses. Moreover, the all-optoelectronic system allows one to gain broadband spectral information by measuring the time-domain THz waveform at each pixel by scanning the detection-pulse delay. However, for such imaging applications where spectral information is not desired, the fs-approach comes at the price of having to scan the delay to find the peak field signal for each pixel. Hence, for many applications, e.g., long-range standoff imaging of objects with depth variation on the scale of millimeters to centimeters, this can significantly reduce the acquisition rate.

## IV. THz Focal Plane Arrays

Coming back to electronic techniques of THz detection, we now address monolithically integrated receiver arrays suitable for room temperature operation.

It was often expected and hoped that high-sensitivity detector arrays would be developed on the basis of Schottky diodes, especially considering that they cannot only be used as power detectors but are also suitable for heterodyne detection. Until now, however, fabrication of such arrays suffers from an insufficient yield and significant performance fluctuations, although this situation may be changing gradually [61].

In 2005 and 2006, two unrelated developments gave the search for cost-effective and high-performance arrays a push into new and somewhat unexpected directions. The first development relates to detectors of infrared radiation. The group of Q. Hu at the Massachusetts Institute of Technology found out that microbolometer arrays, made for the detection of infrared radiation, are surprisingly good detectors of radiation with a frequency of several THz, emitted from quantum-cascade lasers and molecular gas lasers [62], [63]. These findings have initiated numerous activities, e.g., at LETI, Grenoble, aimed at the optimization of microbolometers for the THz frequency regime [64]. Also other types of IR sensor, such as pyroelectric detectors, are now explored more vigorously [65].

The second development, which has triggered our work outlined below, relates to Si CMOS field-effect transistors (FETs). The group of W. Knap, Montpellier, investigated unoptimized commercial MOSFETs as THz detectors. They had performed similar studies with III/V-based transistors before, but the investigation of the MOSFETs was the first where the responsivity and the NEP were determined tentatively [66]. The numbers obtained indicated much promise for further development.

### A. SI FET-Based THz FPAs

The physical mechanism underlying this novel path towards real-time-capable FPAs is rectification of the THz signal in the FET. To our knowledge, it was the work of Diakonov and Shur [67], which, for the first time, drew attention to rectification of high-frequency signals whose frequency exceeds the FET's transit-time-limited cutoff frequency. They considered the possibility of plasma resonances in the gated two-dimensional electron gas of the submicrometer-long transistor channels. Although the excitation of collective plasma oscillations had been an object of intensive studies for quite a long time [68], a novelty of the Diakonov-Shur approach was the prediction that the existence of plasmonic resonances should also manifest itself in the device's DC properties. This prediction ignited considerable interest to search for plasmon-based rectification phenomena in various implementations of FETs by simply measuring a THz-field-induced potential difference between the source and drain terminals.

In the meantime, the theory of detection had been refined for various modalities of electron transport with one of them being the so-called case of strongly damped plasmon excitation, also termed the nonresonant limit of plasmonic mixing [69]. This operation regime was then found by Knap's group to be relevant for Si MOSFETs with a gate longer than 100 nm and operated at room temperature. For this regime, a good sensitivity to THz radiation was reported. NEP values of the order of 100 pW/$\sqrt{\text{Hz}}$ [66] were estimated, which are quite comparable to those of many other practical power detectors operating in the THz frequency range [70].

References [70] and [71] later pointed out that plasma-wave-based rectification in the nonresonant limit can be understood to be an extension of classical resistive mixing, well-known in microelectronics. Resistive mixing is based on the quasi-stationary behavior of FETs; if extended to the non-quasi-stationary case, plasma-wave excitation has to be included. The relationship to resistive mixing is reflected now in the newly coined term of *distributed resistive (self-)mixing*.

The experimental results led to the first demonstration of imaging with transistors above their cutoff frequency, in this case employing GaAs HEMTs [72]. It followed the first dedicated attempt to fabricate monolithically integrated FPAs, where each detector pixel contained an on-chip integrated antenna, a differential pair of FETs and an amplifier, with a commercial foundry process [70], [71], [73], [74]. Fig. 18 shows a photograph and some layout information of the best detectors of these first designs which were fabricated with a 250-nm (Bi)CMOS process. For these detectors of 0.65-THz radiation, a responsivity of 80 kV/W and a NEP of 300 pW/$\sqrt{\text{Hz}}$ were obtained.

In the meantime, various commercial Si process technologies and different circuit designs have been explored. Two papers report significantly improved performance. First, an implementation of this detection principle in a high-end 65-nm

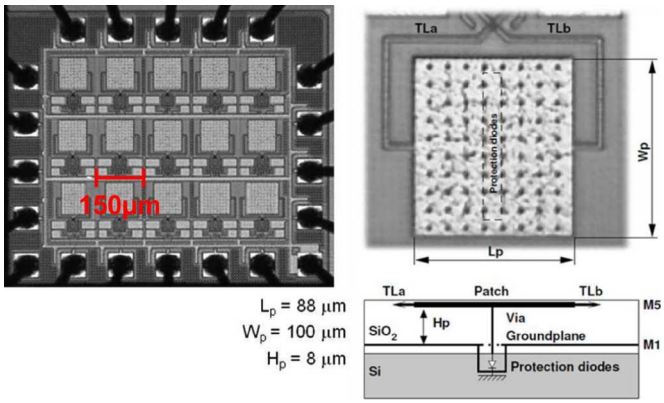


Fig. 18. Left side: 3 × 5-pixel FPA for the detection of 0.65-THz radiation. Top right side: one of the patches of the array. The transmission lines (TLa and TLb) guiding the THz signals to the FETs are visible. Bottom right: Cross section through a patch antenna. Image data from [71].

CMOS-on-SOI technology allowed to reach NEP values as low as 50 pW/$\sqrt{\text{Hz}}$ [75]. The applied design has room for improvement. A second paper reports slightly better NEP values of 43 pW/$\sqrt{\text{Hz}}$; in this case, a more relaxed and significantly less costly 150-nm CMOS technology was used [76]. It is worth remarking that, in the lowest-order approximation of the transport models, the detector's responsivity does not depend on channel length, which partially explains why a very similar NEP of about 50 pW/$\sqrt{\text{Hz}}$ can be achieved using different channel lengths.

It is important to note, that the detection principle is entirely based on the field effect, and not on real carrier transport, thus the high-frequency limit is determined by dielectric relaxation time which typically lies in the range of several THz and strongly exceeds the transistor's cutoff frequency. The latter represents an ultimate limiting factor for signal modulation frequencies [77] or the response time. Therefore, in contrast to thermal-time-limited detectors with similar NEP, FET-based detectors allow modulation speeds reaching up to 1 MHz and above (limited by capacitive loading because of the high impedance of the transistor's channel [70], [78]). In their high speed, they are similar to Schottky diode detectors.

This property allows to increase the sensitivity of the FETs by application of the heterodyne detection principle. We demonstrated heterodyne imaging with a 0.65-THz emitter [79], [80]. As LO, we employed a second radiation source which was phase-locked to the first one. The radiation of the first source was focused to illuminate the object which was raster scanned through the focus. The transmitted radiation was then overlaid with that from the LO at a beam combiner, guided to the detectors, and distributed over the entire FPA. We estimate that each FET detector received only 2 $\mu$W of LO power, far less than needed for optimal performance [80]. This was sufficient, however, to improve the dynamic range by 29 dB [79]. The NEP was estimated to be 8 fW/Hz ($-112$ dBm/Hz).

The improvement of the contrast can be seen from the imaging data shown in Fig. 19. It presents data of transmission measurements through a paper envelope containing a dextrose tablet. In power-detection mode (radiation from LO source blocked), the received signal is weak, and details such as the central notch of the tablet are nearly invisible. In heterodyne mode, the considerably higher contrast permits to clearly identify the notch. The writing on the tablet can be noticed, although the image shown here does not allow to discern individual characters. In addition to the improvement in sensitivity, a heterodyne approach gives access to the information on the THz phase which can be used for reconstruction of depth information, hence offers some 3-D imaging capabilities. An illustration of this aspect is given in Fig. 20, which presents the power and the phase information obtained by a heterodyne scan (single scan, 10-ms integration time per pixel) of a leaf of a ficus tree. The processed phase information renders a pseudo-3D representation of the leaf.

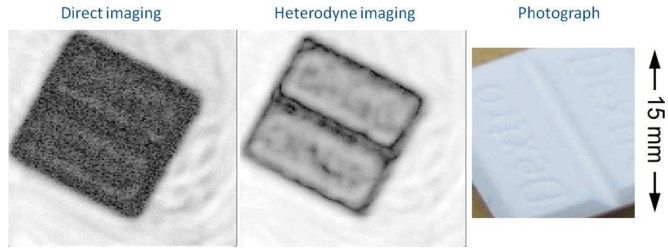


Fig. 19. THz image taken through a dextrose tablet (see photograph on the right side) hidden in a letter envelope. Left side: Detection of transmitted power alone; middle: heterodyne measurement. The measurements were taken with two FET detectors in parallel, the object was raster-scanned.

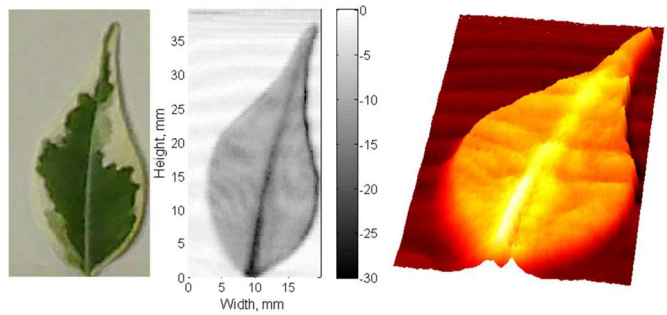


Fig. 20. Transmission image of a freshly cut leaf of a *ficus benjamina*, at 592 GHz. Left panel: photograph of the leaf; middle panel: transmitted-power image; right panel: pseudo-3D image obtained after unwrapping of the phase information. Image data from [81]. The measurements were taken with a single FET detector, the object was propagated in $x$–$y$-direction for raster scanning.

### *B. Summary and Potential of Si FET-Based THz FPAs*

We point out that, until now, all images have been taken in raster scan mode, albeit with fairly short integration time in the ms to 10-ms range. Currently, we and others are working towards real-time implementations of MOSFET-based imaging. This requires both a large number of pixel, distributed over an area of the FPA of several to many cm$^2$, and implementation of a proper readout electronics.

Based on the data given above, we can estimate the expected performance of an FPA for 600 GHz in heterodyne mode. Assuming a power of 0.5 mW of each the LO and the THz imaging beam directly in front of the FPA, and further assuming equal distribution of this power across it (containing 256 × 256 detectors over an area of $50 \times 50$ mm$^2$), then a dynamic range of 30 dB would be achieved at 30-Hz frame rate.

In many real applications, the power of the THz imaging beam at the FPA is likely to be lower, as 1 mW is about the maximum available source power at 600 GHz today (considering oscillator-multiplier sources; backward-wave oscillators may provide somewhat more). Coupling and imaging losses have to be taken into account. Furthermore, one of the challenges for the success of an imaging technology with monolithically integrated FPAs is the large wavelength of THz radiation (1 THz corresponding to $\lambda_{\mathrm{vac}} = 300\ \mu$m). Diffraction aspects suggest that a FPA with a large number of monolithically integrated pixels is more practical at high frequencies (0.5 THz and above) and in conjunction with large numerical-aperture optics, while its usefulness is questionable at frequencies approaching 100 GHz. FPAs based on CMOS FETs will be used at first for short-distance, high-resolution imaging, rather than compete with all-electronic imaging approaches of standoff security scanners.

The FET FPAs investigated until now have been designed for narrowband operation. The underlying detection principle is not of resonant nature, though. The bandwidth limitation results from the choice of the integrated antenna. The future will certainly see the development of broadband FET detectors, e.g., for FMCW purposes or spectroscopic applications.

Finally, we mention that rectification cannot only be achieved with FETs, but also with heterobipolar transistors (HBTs) [82]. This was tested with $n-p-n$ SiGe HBTs which were fabricated with a $\mathrm{f}_{\mathrm{max}} = 220$-GHz SiGe:C process. Each pixel contained a monolithically integrated folded-dipole antenna for 645 GHz, but no integrated amplifier. While the measured responsivity (850 V/W) at 645 GHz was comparable to that of FETs, the NEP was, with minimum values in the range of 30 $\mathrm{nW}/\sqrt{\mathrm{Hz}}$, inferior by nearly three orders of magnitude. The main reason being that—unlike the case of FETs—detector operation of HBTs requires an emitter-collector current, which introduces significant noise. From this point of view, HBTs do not appear to be an attractive alternative to FETs and HEMTs. However, an interesting subharmonic mixing approach, detecting 650-GHz radiation by mixing with the fourth subharmonic at about 162 GHz, has recently been demonstrated with them [83]. Subharmonic mixing may help to render heterodyne detection of THz radiation more practical and less cost-intensive because it alleviates the need for additional power sources as LOs at the fundamental frequency.

## V. Conclusion and Outlook

This paper has introduced respectively reviewed five novel THz imaging modalities. The main thrust of the work has been to identify viable approaches of parallel multi-pixel detection with the goal to achieve real-time imaging capabilities.

Of the THz imaging systems described in this paper, the all-electronic 812-GHz imager with mechanical scanning has already demonstrated operation close to real-time mode, albeit with limited dynamic range. The second all-electronic system—combining synthetic-aperture techniques and mechanical scanning with range determination by FMCW sweeping in the range of 220–320 GHz—is designed to achieve several frames per second, but this could not yet be reached because of the limited output power and sensitivity of the components at 220–320 GHz. Therefore, a similar system will be realized at 75–110 GHz within the new LiveDetect3D project. We have verified already that components show sufficient dynamic range so that real-time operation should be possible even with a 10-m working distance.

The two laser-based approaches, which employ EO THz-NIR conversion to permit multi-pixel detection with NIR cameras (i.e., either homodyne detection with a CCD or heterodyne detection with a PMD), still have a way to go before they reach a frame-rate of 1 fps and more. They are attractive because they can principally cover a significant portion of the THz frequency regime (hundreds of GHz to at least several THz) and thus may well be able to combine imaging with spectroscopic distinction of objects. However, camera-based multi-pixel detection for the (quasi-)CW systems still requires improvement. THz-OPO-based imaging would benefit enormously from an OPO with higher peak power than was available here, while the approach using a time-of-flight camera needs a camera with faster readout. For both systems, noise suppression leaves room for optimization.

The fifth system, again an electronic one, employs a monolithically integrated Si MOSFET FPA for detection around 600 GHz (but the approach is also principally capable of broadband operation). The focus of the work has been on optimization of the performance of these novel detectors. The results are favorable and strongly suggest, that the near future will see implementation of larger FPAs with suitable camera readout for imaging at high frame-rates.

In summary, the capability to capture THz images of actively illuminated scenes in or close to real time has progressed significantly. We have identified promising approaches which exploit various ways of multi-pixel parallel detection. With the exception of the silicon CMOS FPA, which also allows direct power detection, all approaches employ coherent detection for better noise suppression, either in homodyne mode, or via heterodyne mixing for additional enhancement of the sensitivity. It has become clear that the limited available THz power for scene illumination necessitates to push sensitivity enhancement and noise suppression in the detectors to their limits in order to achieve real-time operation of imaging with good dynamic range. We have identified ways for specific improvements for each of the various approaches which now have to be implemented.

## Acknowledgment

The authors would like thank TOPTICA GmbH, Munich; Xiton GmbH, Kaiserslautern; D. Molter, J. Jonuscheit, and R. Beigang of the Fraunhofer-Institut IPM, Kaiserslautern; and J. Dall, A. Kusk, V. Zhurbenko, and T. Jensen of Denmark Technical University for their contributions.

## References

[1] H.-B. Liu, H. Zhong, N. Karpowicz, Y. Chen, and X.-C. Zhang, "Terahertz spectrosopy and imaging for defense and security applications," *Proc. IEEE*, vol. 95, pp. 1514–1527, 2007.

[2] B. M. Fischer, Y. Demarty, M. Schneider, T. Löffler, A. Keil, and H. Quast, "THz all-electronic 3-D imaging for safety and security applications," in *Proc. SPIE*, 2010, vol. 7671, pp. 767111–767111-7.

[3] A. G. Davies, A. D. Burnett, W. H. Fan, E. H. Linfield, and J. E. Cunningham, "Terahertz spectroscopy of explosives and drugs," *Mater. Today*, vol. 11, pp. 18–26, 2008.

[4] N. Krumbholz, T. Hochrein, N. Vieweg, T. Hasek, K. Kretschmer, M. Bastian, M. Mikulic, and M. Koch, "Monitoring polymeric compounding processes inline with THz time-domain spectroscopy," *Polymer Test.*, vol. 28, pp. 30–35, 2009.

[5] N. Hasegawa, T. Löffler, M. Thomson, and H. G. Roskos, "Remote identification of protrusions and dents on surfaces by terahertz reflectometry with spatial beam filtering and out-of-focus detection," *Appl. Phys. Lett.*, vol. 83, pp. 3996–3998, 2003.

[6] D. Banerjee, W. von Spiegel, M. D. Thomson, S. Schabel, and H. G. Roskos, "Diagnosing water content in paper by terahertz radiation," *Opt. Exp.*, vol. 16, no. 12, pp. 9060–9066, 2008.

[7] K. Kawase, T. Shibuya, S. Hayashi, and K. Suizu, "THz imaging techniques for nondestructive inspections," *Comptes Rendus Physique*, vol. 11, pp. 510–518, 2010.

[8] B. Hils, M. D. Thomson, T. Löffler, W. von Spiegel, C. am Weg, H. G. Roskos, P. de Maagt, D. Doyle, and R. D. Geckeler, "Terahertz profilometry at 600 GHz with 0.5 $\mu$m depth resolution," *Opt. Exp.*, vol. 16, pp. 11289–11293, 2008.

[9] A. Roggenbuck, H. Schmitz, A. Deninger, I. C. Mayorga, J. Hemberger, R. Gsten, and M. Grüninger, "Coherent broadband continuous-wave terahertz spectroscopy on solid-state samples," *New J. Phys.*, vol. 12, p. 043017, 2010.

[10] C. J. Strachan, P. F. Taday, D. A. Newnham, K. C. Gordon, J. A. Zeitler, M. Pepper, and T. Rades, "Using terahertz pulsed spectroscopy to quantify pharmaceutical polymorphism and crystallinity," *J. Pharmaceut. Sci.*, vol. 94, pp. 837–846, 2005.

[11] M. Nagel, F. Richter, P. Haring Bolívar, and H. Kurz, "A functionalized THz sensor for marker-free DNA analysis," *Phys. Med. Biol.*, vol. 48, pp. 3625–3636, 2003.

[12] K. B. Cooper, R. J. Dengler, N. Llombart, A. Talukder, A. V. Panangadan, C. S. Peay, I. Mehdi, and P. H. Siegel, "Fast, high-resolution terahertz radar imaging at 25 meters," in *Proc. SPIE*, 2010, vol. 7671, p. 76710Y.

[13] K. B. Cooper, R. J. Dengler, G. Chattopadhyay, E. Schlecht, A. Skalare, I. Mehdi, and P. H. Siegel, "Penetrating 3-D imaging at 4- and 25-m range using a submillimeter-wave radar," *IEEE Microw. Theory Tech.*, vol. 56, no. 12, pp. 2771–2778, 2008.

[14] B. Pradarutti, R. Müller, G. Matthäus, C. Brückner, S. Riehemann, G. Notni, S. Nolte, and A. Tünnermann, "Multichannel balanced electrooptic detection for terahertz imaging," *Opt. Exp.*, vol. 15, pp. 17652–17660, 2007.

[15] B. Pradarutti, R. Müller, W. Freese, G. Matthäus, S. Riehemann, G. Notni, S. Nolte, and A. Tünnermann, "Terahertz line detection by a microlens array coupled photoconductive antenna array," *Opt. Exp.*, vol. 16, pp. 18443–18450, 2008.

[16] J. M. Dai, J. Liu, and X.-C. Zhang, "Terahertz wave air photonics: Terahertz wave generation and detection with laser-induced gas plasma," *IEEE J. Sel. Topics Quantum Electron.*, vol. 17, no. 1, pp. 183–190, 2011.

[17] G. Malcolm, "Terahertz laser sources based on optical parametric oscillators," presented at the 6th Optoelectron. Photon. Winter School, , Fai della Paganella, Italy, Feb. 20–26, 2011.

[18] S. Wohnsiedler, M. Theuer, M. Herrmann, S. Islam, J. Jonuscheit, R. Beigang, and F. Hase, "Simulation and experiment of terahertz standoff detection," in *Proc. SPIE*, 2009, vol. 7215, p. 72150H.

[19] W. von Spiegel, C. amWeg, R. Henneberger, R. Zimmermann, T. Löffler, and H. G. Roskos, "Active THz imaging system with improved frame rate," in *Proc. SPIE*, 2009, vol. 7311, p. 73110O.

[20] W. von Spiegel, C. am Weg, R. Henneberger, R. Zimmermann, and H. G. Roskos, "Illumination aspects in active terahertz imaging," *IEEE Trans. Microw. Theory Tech.*, vol. 58, pp. 2008–2013, 2010.

[21] C. am Weg, W. von Spiegel, R. Henneberger, R. Zimmermann, T. Löffler, and H. G. Roskos, "Quasioptical system design," in *Proc. SPIE*, 2009, vol. 7215, p. 72150R.

[22] C. am Weg, W. von Spiegel, R. Henneberger, R. Zimmermann, T. Löffler, and H. G. Roskos, "Fast active THz cameras with ranging capabilities," *J. Infrared Millim. THz Waves*, vol. 30, pp. 1281–1296, 2009.

[23] C. am Weg, W. von Spiegel, R. Henneberger, R. Zimmermann, T. Löffler, and H. G. Roskos, "Fast active THz camera with range detection by frequency modulation," in *Proc. SPIE*, 2009, vol. 7215, p. 72150F.

[24] M. C. Kemp, "Millimetre wave and terahertz technology for the detection of concealed threats a review," in *Proc. SPIE*, 2006, vol. 6402, p. 64020D.

[25] V. Krozer, T. Löffler, J. Dall, A. Kusk, F. Eichhorn, R. K. Olsson, J. D. Buron, P. U. Jepsen, V. Zhurbenko, and T. Jensen, "THz imaging systems with aperture synthesis techniques," *IEEE Trans. Microw. Theory Tech.*, vol. 58, pp. 2027–2039, 2010.

[26] K. Miyashiro, J. Schellenberg, J. Loveberg, V. Kolinko, and J. McCoy, "An E-band electronically scanned imaging radar system," in *Proc. IMS, IEEE/MTT-S Int. Microw. Symp.*, 2007, pp. 1459–1462.

[27] V. Manasson, L. Sadovnik, R. Mino, and S. Rodionov, "Novel passive millimeter-wave imaging system: Prototype fabrication and testing," in *Proc. SPIE*, 2000, vol. 4032, pp. 2–13.

[28] A. Natarajan, A. Komijani, X. Guan, A. Babakhani, Y. Wang, and A. Hajimiri, "A 77GHz phased-array transmitter with local LOPath phase-shifting in silicon," *IEEE J. Solid-State Circuits*, vol. 41, pp. 2795–2806, Dec. 2006.

[29] L. Schulwitz and A. Mortazawi, "A compact dual-polarized multibeam phased-array architecture for millimeter-wave radar," *IEEE Trans. Microw. Theory Tech.*, vol. 53, no. 11, pp. 3588–3594, Nov. 2005.

[30] N. Skou and D. Le Vine, *Microwave Radiometer Systems; Design and Analysis*. Norwood, MA: Artech House, 2006.

[31] C. S. Ruf, "Numerical annealing of low-redundancy linear arrays," *IEEE Trans. Antenna Propag.*, vol. 41, no. 1, pp. 85–90, 1993.

[32] A. F. Yegulalp, "Fast backprojection algorithm for synthetic aperture radar," in *IEEE Radar Conf. Rec.*, 1999, pp. 60–65.

[33] S. Basu and Y. Bresler, "O(N3logN) backprojection algorithm for Radon transform," *IEEE Trans. Med. Imag.*, vol. 21, no. 2, pp. 76–88, 2002.

[34] L. M. H. Ulander, H. Hellsten, and G. Stenström, "Synthetic-aperture radar processing using fast factorized back-projection," *IEEE Trans. Aerosp. Electron. Systems*, vol. 39, no. 3, pp. 760–776, 2003.

[35] Q. Wu, T. D. Hewitt, and X.-C. Zhang, "Two-dimensional electro-optic imaging of THz beams," *Appl. Phys. Lett.*, vol. 69, pp. 1026–1028, 1996.

[36] T. Yasuda, Y. Kawada, H. Toyoda, and H. Takahashi, "Terahertz movies of internal transmission images," *Opt. Exp.*, vol. 15, pp. 15583–15588, 2007.

[37] A. Nahata, J. T. Yardley, and T. F. Heinz, "Two-dimensional imaging of continuous-wave terahertz radiation using electro-optic detection," *Appl. Phys. Lett.*, vol. 81, pp. 963–965, 2002.

[38] K. Kawase, Y. Ogawa, H. Minamide, and H. Ito, "Terahertz parametric sources and imaging applications," *Semicond. Sci. Technol.*, vol. 20, pp. S258–S265, 2005.

[39] T. J. Edwards, D. Walsh, M. B. Spurr, C. F. Rae, M. H. Dunn, and P. G. Browne, "Compact source of continuously and widely-tunable terahertz radiation," *Opt. Exp.*, vol. 14, pp. 1582–1589, 2006.

[40] G. Zhao, R. N. Schouten, N. van der Valk, W. T. Wenckebach, and P. C. M. Planken, "Design and performance of a THz emission and detection setup based on a semi-insulating GaAs emitter," *Rev. Sci. Instrum.*, vol. 73, pp. 1715–1719, 2002.

[41] A. Dreyhaupt, S. Winnerl, T. Dekorsy, and M. Helm, "High-intensity terahertz radiation from a microstructured large-area photoconductor," *Appl. Phys. Lett.*, vol. 86, p. 121114, 2005.

[42] T. Löffler, M. Kreß, M. Thomson, T. Hahn, N. Hasegawa, and H. G. Roskos, "Comparative performance of terahertz emitters in amplifier-laser-based systems," *Semicond. Sci. Technol.*, vol. 20, pp. S134–S141, 2005.

[43] T. Bartel, P. Gaal, K. Reimann, M. Woerner, and T. Elsaesser, "Generation of single-cycle THz transients with high electric-field amplitudes," *Opt. Lett.*, vol. 30, p. 28052807, 2005.

[44] M. D. Thomson, V. Blank, and H. G. Roskos, "Terahertz white-light pulses from an air plasma photo-induced by incommensurate two-color optical fields," *Opt. Exp.*, vol. 18, pp. 23173–23182, 2010.

[45] F. Meng and D. Molter *et al.*, "THz imaging with a THz-OPO and a CMOS camera,", unpublished.

[46] F. Z. Meng, D. Thomson, D. Molter, T. Löffler, J. Bartschke, T. Bauer, M. Nittmann, and H. G. Roskos, "Coherent electro-optical detection of THz radiation from an optical parametric oscillator," *Opt. Exp.*, vol. 18, pp. 11316–11326, 2010.

[47] D. Molter, M. Theuer, and R. Beigang, "Nanosecond terahertz optical parametric oscillator with a novel quasi-phase matching scheme in lithium niobate," *Opt. Exp.*, vol. 17, pp. 6623–6628, 2009.

[48] T. Bauer, J. S. Kolb, T. Löffler, E. Mohler, H. G. Roskos, and U. C. Pernisz, "Indium-tin-oxide-coated glass as dichroic mirror for far-infrared electromagnetic radiation," *J. Appl. Phys.*, vol. 92, pp. 2210–2212, 2002.

[49] F. Meng, M. D. Thomson, V. Blank, W. von Spiegel, T. Löffler, and H. G. Roskos, "Characterizing large-area electro-optic crystals toward two-dimensional real-time terahertz imaging," *Appl. Opt.*, vol. 48, p. 51975204, 2009.

[50] Q. Wu and X.-C. Zhang, "Free-space electro-optic sampling of terahertz beams," *Appl. Phys. Lett.*, vol. 67, pp. 3523–3525, 1995.

[51] T. Löffler, T. May, C. am Weg, A. Alcin, B. Hils, and H. G. Roskos, "Continuous-wave terahertz imaging with a hybrid system," *Appl. Phys. Lett.*, vol. 90, p. 091111, 2007.

[52] T. May, C. am Weg, A. Alcin, B. Hils, T. Löffler, and H. G. Roskos, "Towards an active real-time THz camera: First realization of a hybrid system," in *Proc. SPIE*, 2007, vol. 6549, p. 654907.

[53] F. Friederich, G. Schuricht, A. Deninger, F. Lison, G. Spickermann, P. Haring Bolivar, and H. G. Roskos, "Phase-locking of the beat signal of two distributed-feedback lasers to oscillators working in the MHz to THz range," *Opt. Exp.*, vol. 18, pp. 8621–8629, 2010.
[54] PMDtec. Siegen, Germany [Online]. Available: http://www.pmdtec.com
[55] G. Spickermann, F. Friederich, H. G. Roskos, and P. Haring Bolívar, "A high signal-to-noise ratio electrooptical THz imaging system based on an optical demodulating detector array," *Opt. Lett.*, vol. 34, pp. 3424–3426, 2009.
[56] F. Friederich, G. Spickermann, A. Roggenbuck, A. Deninger, C. am Weg, W. von Spiegel, F. Lison, P. Haring Bolivar, and H. G. Roskos, "Hybrid continuous-wave demodulating multipixel terahertz imaging systems," *IEEE Trans. Microw. Theory Tech.*, vol. 58, no. 7, pp. 2022–2026, 2010.
[57] T. Ringbeck, T. Möller, and B. Hagebeuker, "Multidimensional measurement by using 3-D PMD sensors," *Adv. Radio Sci.*, vol. 5, pp. 135–146, 2007.
[58] T. Ringbeck, "A 3-D time of flight camera for object detection," presented at the 8th Conf. Optical 3-D Meas. Tech., ETH Zurich, Switzerland, Jul. 2007.
[59] G. Gallot and D. Grischkowsky, "Electro-optic detection of terahertz radiation," *J. Opt. Soc. Amer. B*, vol. 16, pp. 1204–1212, 1999.
[60] Z. Jiang, F. G. Sun, and Q. Chen, "Electro-optic sampling near zero optical transmission point," *Appl. Phys. Lett.*, vol. 74, pp. 1191–1193, 1999.
[61] M. Ortolani, A. Di Gaspare, and R. Casini, "Progress in producing terahertz detector arrays," in *SPIE Newsroom*, Feb. 14, 2011, 10.1117/2.1201101.003449.
[62] A. W. M. Lee and Q. Hu, "Real-time, continuous-wave terahertz imaging by use of a microbolometer focal-plane array," *Appl. Phys. Lett.*, vol. 30, pp. 2563–2565, 2005.
[63] A. W. M. Lee, Q. Qin, S. Kumar, B. S. Williams, and Q. Hu, "Real-time terahertz imaging over a standoff distance ( $>$25 meters)," *Appl. Phys. Lett.*, vol. 89, p. 141125, 2006.
[64] F. Simoens, T. Durand, J. Meilhan, P. Gellie, W. Maineult, C. Sirtori, S. Barbieri, H. Beere, and D. Ritchie, "Terahertz imaging with a quantum cascade laser and amorphous-silicon microbolometer array," in *Proc. SPIE*, 2009, vol. 7485, p. 74850M.
[65] Q. Li, S.-H. Ding, R. Yao, and Q. Wang, "Real-time terahertz scanning imaging by use of a pyroelectric array camera and image denoising," *J. Opt. Soc. Amer. A*, vol. 27, pp. 2381–2386, 2010.
[66] R. Tauk, F. Teppe, S. Boubanga, D. Coquillat, W. Knap, Y. M. Meziani, C. Gallon, F. Boeuf, T. Skotnicki, T. Skotnicki, C. Fenouillet-Beranger, D. K. Maude, S. Rumyantsev, and M. S. Shur, "Plasma wave detection of terahertz radiation by silicon field effects transistors: Responsivity and noise equivalent power," *Appl. Phys. Lett.*, vol. 89, p. 253511, 2006.
[67] M. Dyakonov and M. Shur, "Detection, mixing, and frequency multiplication of terahertz radiation by two-dimensional electronic fluid," *IEEE Trans. Electron Devices*, vol. 43, no. 3, pp. 380–387, 1996.
[68] S. J. Allen, D. C. Tsui, and R. A. Logan, "Observation of the two-dimensional plasmon in silicon inversion layers," *Phys. Rev. Lett.*, vol. 38, p. 980983, 1977.
[69] W. Knap, V. Kachorovskii, Y. Deng, S. Rumyantsev, J.-Q. Lü, R. Gaska, M. S. Shur, G. Simin, X. Hu, M. Asif Khan, C. A. Saylor, and L. C. Brunel, "Nonresonant detection of terahertz radiation in field effect transistors," *J. Appl. Phys.*, vol. 91, pp. 9346–9353, 2002.
[70] A. Lisauskas, U. Pfeiffer, E. Öjefors, P. Haring Bolivar, D. Glaab, and H. G. Roskos, "Rational design of high-responsivity detectors of terahertz radiation based on distributed self-mixing in silicon field-effect transistors," *J. Appl. Phys.*, vol. 105, p. 114511, 2009.
[71] E. Öjefors, U. Pfeiffer, A. Lisauskas, and H. G. Roskos, "A 0.65 THz focal-plane array in a quarter-micron CMOS process technology," *IEEE J. Solid-State Circuits*, vol. 44, pp. 1968–1976, 2009.
[72] A. Lisauskas, W. von Spiegel, S. Boubanga-Tombet, A. El Fatimy, D. Coquillat, F. Teppe, N. Dyakonova, W. Knap, and H. G. Roskos, "Terahertz imaging with GaAs field-effect transistors," *Electron. Lett.*, vol. 44, pp. 408–409, 2008.
[73] A. Lisauskas, D. Glaab, H. G. Roskos, E. Öjefors, and U. Pfeiffer, "Terahertz imaging with Si MOSFET focal-plane arrays," in *Proc. SPIE.*, 2009, vol. 7215, p. 72150.
[74] E. Öjefors, A. Lisauskas, D. Glaab, H. G. Roskos, and U. R. Pfeiffer, "Terahertz imaging detectors in CMOS technology," *J. Infrared Millim. THz Waves*, vol. 30, pp. 1269–1280, 2009.
[75] E. Öjefors, N. Baktash, Y. Zhao, R. Al Hadi, H. Sherry, and U. R. Pfeiffer, "Terahertz imaging detectors in a 65-nm CMOS SOI technology," in *Proc. ESSCIRC*, Seville, Spain, Sep. 2010, pp. 486–489.
[76] S. Boppel, A. Lisauskas, V. Krozer, and H. G. Roskos, "Performance and performance variations of sub-1-THz detectors fabricated with a 0.15-m CMOS foundry process," *Electron. Lett.*, vol. 47, no. 11, May 26, 2011.
[77] W. J. Stillman and M. S. Shur, "Closing the gap: Plasma wave electronic terahertz detectors," *J. Nanoelectron. Optoelectron.*, vol. 2, pp. 209–221, 2007.
[78] W. Stillman, M. S. Shur, D. Veksler, S. Rumyantsev, and F. Guarin, "Device loading effects on nonresonant detection of terahertz radiation by silicon MOSFETs," *Electron. Lett.*, vol. 43, pp. 422–423, 2007.
[79] D. Glaab, S. Boppel, A. Lisauskas, U. Pfeiffer, E. Öjefors, and H. G. Roskos, "Terahertz heterodyne detection with silicon field-effect transistors," *Appl. Phys. Lett.*, vol. 96, p. 042106, 2010.
[80] U. Pfeiffer, E. Öjefors, A. Lisauskas, D. Glaab, and H. G. Roskos, "A CMOS focal-plane array for heterodyne terahertz imaging," in *Proc. IEEE RFIC Symp.*, 2009, pp. 433–436.
[81] S. Boppel, A. Lisauskas, U. Pfeiffer, E. Öjefors, and H. G. Roskos, "Field effect transistors for power and heterodyne detection of terahertz radiation fabricated in CMOS technology," presented at the NATO SET Panel Meeting SET-159 Terahertz and Other Electromagnetic Wave Techniques for Defence and Security, Vilnius, May 3–4, 2010.
[82] U. R. Pfeiffer, E. Öjefors, A. Lisauskas, and H. G. Roskos, "Opportunities for silicon at mmwave and terahertz frequencies," in *Proc. IEEE Bipolar/BICMOS Circuits and Technology Meeting (BCTM)*, 2008, pp. 149–156.
[83] E. Öjefors and U. R. Pfeiffer, "A 650 GHz receiver front-end for terahertz imaging arrays," in *Proc. IEEE Int. Solid-State Circuits Conf. (ISSCC)*, 2010, pp. 430–432.

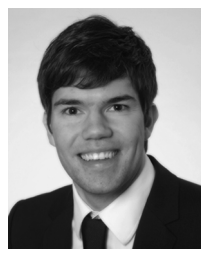

**Fabian Friederich** (M'09) was born in Speyer, Germany, in 1983. He studied optoelectronics at the Aalen University, Germany, where he received the Diploma degree in 2007 for his work on adaptive laser beam shaping for micromaterial processing at the Laser Zentrum Hannover. Since 2007 he has been working towards the Ph.D. degree in the Ultrafast Spectroscopy and Terahertz Physics Group of Goethe-University, Frankfurt am Main, Germany.

His current research involves electrooptic THz imaging and signal processing.

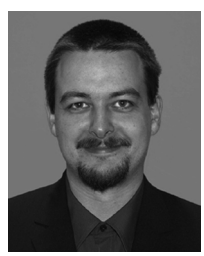

**Wolff von Spiegel** studied physics at the Technical University of Darmstadt, Germany. For his diploma thesis, he worked on laser beam writing for continuously-profiled diffractive optical elements. He received the Ph.D. degree for his work on holographic projection screens from the Technical University of Darmstadt in 2007.

In 2007, he joined the Ultrafast Spectroscopy and Terahertz Physics Group of Goethe-University, Frankfurt am Main, Germany. His current field of work at the University of Frankfurt is terahertz-imaging and -metrology.

**Maris Bauer** was born in Frankfurt am Main, Germany, in 1985. He received the B.Sc. degree in physics from Goethe-University, Frankfurt am Main, Germany, in 2009. His thesis concerned syntheticapertures in terahertz imaging. He is currently working towards the Master's degree in the Ultrafast Spectroscopy and Terahertz Physics Group of Goethe-University.

His current research interests are the design and implementation of inductive mesh bandpass filters for ultra-broadband terahertz spectroscopy.

**Fanzhen Meng** was born in Shandong, China, in 1977. She received the B.A. degree in physics education from Qufu University, China, in 2000, the M.A. degree in physics from Nankai University, Tianjin, China, in 2003, with a thesis on Er:Yb glass lasers, and the Ph.D. degree from the University of Heidelberg, Germany, in 2007, for her work on *in situ* IR spectroscopy of metal nano-particles grown on MgO(001) substrates under ultrahigh-vacuum conditions.

She then joined the Ultrafast Spectroscopy and Terahertz Physics Group of Goethe-University, Frankfurt am Main, as a Postdoctoral Researcher, to develop a THz-OPObased imaging system. She is now with Carl Zeiss AG, Oberkochen.

**Mark D. Thomson** (M'09) received the M.Sc. degree in physics from the University of Auckland, New Zealand, in 1998 and the Ph.D. degree in physics from Goethe-University, Frankfurt am Main, Germany, in 2004. His doctoral research work concerned femtosecond spectroscopy of metallorganic charge-transfer compounds.

He is currently a permanent staff member and team leader in the Ultrafast Spectroscopy and Terahertz Physics group at Goethe-University, concentrating on ultrafast optical, magnetooptical, and THz spectroscopy of molecular and photomagnetic materials. He participates in the development of novel THz instrumentation, such as THz white-light generation in laser-induced air plasmas.

**Sebastian Boppel** was born in Preetz, Germany, in 1982. He graduated in physics from the University of Heidelberg, Germany, in 2008.

Currently, he is working towards Ph.D. degree in physics at the Goethe-University, Frankfurt am Main, Germany, working in the Ultrafast Spectroscopy and Terahertz Physics Group on the topic of CMOS-transistor-based THz detection.

**Alvydas Lisauskas** received the Diploma degree in physics from Vilnius University, Lithuania, in 1995 and the Ph.D. degree from the Royal Institute of Technology, Stockholm, Sweden, in 2001.

In 2001–2002, he was a Senior Researcher with the Semiconductor Physics Institute, Vilnius, Lithuania. Since 2002, he has been a member of the Ultrafast Spectroscopy and Terahertz Physics group of Goethe-University, Frankfurt am Main, Germany, working on fundamental aspects of novel semiconductor devices for THz applications.

**Bernd Hils** was born in Frankfurt am Main, Germany, in 1961. He received the Diploma degree in physics from Goethe-University, Frankfurt am Main, Germany, in 1989.

He is a member of the Ultrafast Spectroscopy and Terahertz Physics group at Goethe-University, concentrating on fundamental aspects of optical metrology using THz radiation.

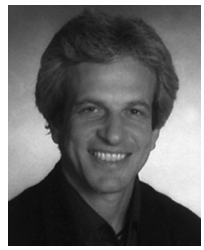

**Viktor Krozer** (M'91–SM'03) received the Dipl.-Ing. and Dr.-Ing. degrees in electrical engineering from the Technical University of Darmstadt (TU Darmstadt), Darmstadt, Germany, in 1984 and 1991, respectively.

In 1991, he became a Senior Scientist with TU Darmstadt, where he was involved with high-temperature microwave devices and circuits and submillimeter-wave electronics. From 1996 to 2002, he was a Professor at the Technical University of Chemnitz, Germany. From 2002 to 2009, he was a Professor with Electromagnetic Systems, DTU Elektro, Technical University of Denmark, Copenhagen, Denmark, and was Head of the Microwave Technology Group. Since 2009, he has been the endowed Oerlikon-Leibniz-Goethe Professor for Terahertz Photonics at Goethe-University, Frankfurt am Main, Germany. His research areas include terahertz electronics, monolithic microwave integrated circuits, nonlinear circuit analysis and design, device modeling, and remote sensing instrumentation.

**Andreas Keil** was born in Kiel, Germany, in 1975. He received the Diploma degree in physics from the Christian Albrechts University, Kiel, Germany, in 2003 and the Ph.D. degree from the National University of Singapore, in the field of quantum information.

Since 2008, he has been with the SynView GmbH, Bad Homburg, Germany. Currently, his main research interests are terahertz imaging and high-performance computation.

**Torsten Löffler** was born in Winterberg, Germany, in 1970. He received the Diploma degree in physics from RWTH Aachen, Aachen, Germany, and the Ph.D. degree from Goethe-University, Frankfurt am Main, Germany, in 2003, based on research in the Ultrafast Spectroscopy and Terahertz Physics Group.

Based on his subsequent research as a Postdoctoral Researcher, he founded Loeffler Technology GmbH (LTG) in 2007 to commercialize THz technology and to develop the first products. In January 2009, LTG became SynView GmbH, Frankfurt, Germany, to enter the industrial nondestructive testing market. He holds several patents and has authored or coauthored more than 50 publications, most of them on THz technology. At SynView GmbH, he is focusing on the technology and product development as well as the technical evaluation of potential applications. In addition, he serves the scientific customers and leads all publicly funded projects.

**Ralf Henneberger** received the Diploma degree in physics from the University of Bonn, Germany, in 1994, for research on avalanche photodiodes for scintillating crystal readout.

In 1994, he also joined Radiometer Physics GmbH as System Engineer and QA manager. He has experience with the 3D-simulation of waveguide multipliers based on planar Schottky diodes, the design, fabrication and testing of multiplier chains for the LO-subsystem of the Herschel/Planck satellite, as well as the design and development of cryogenic transmitter/receiver systems. He is also involved with QA/PA management for space projects.

**Anna Katharina Huhn** was born in Kirchen, Germany, in 1982. She studied electrical engineering from 2001 to 2008 at the University of Siegen, Siegen, Germany, where she received the Diploma degree in 2008 for a thesis on broadband terahertz spectroscopy.

Since then, she has been a Researcher at the Institute of High Frequency and Quantum Electronics at the University of Siegen. She is working on the development of fully electronic terahertz imaging systems and on broadband terahertz material characterization especially of energetic materials.

**Gunnar Spickermann** was born in Siegen, Germany, in 1979. In 1999, he began his computer engineering studies at the University of Siegen, Siegen, Germany, where he received the Diploma degree in 2005 for his work on the development of a characterization tool for microfluidic devices comprising optoelectronics.

Since then, he has been a Researcher at the Institute of High Frequency and Quantum Electronics at the University of Siegen, where he is developing electrooptic terahertz imaging systems, especially in conjunction with the demodulating PMD camera.

**Peter Haring Bolívar** was born in Mexico City, Mexico, in 1969. He studied electrical engineering from 1987 to 1992 at the RWTH Aachen University, Aachen, Germany.

From 1992 to 1993, he was head of the Rescue Equipment Division at Nautica Diesel Europea, Mexico City. From 1993 to 1996, he worked as a Scientific Assistant at the Institut für Halbleitertechnik II of the RWTH Aachen on conjugated polymers and femtosecond dynamics in semiconductors. From 1997 to 2001, he was head of ultra-high-frequency research at the Institut of Semiconductor Electronics at the RWTH Aachen. From 2001 to 2004, he was head of research at this institution with activities in the fields of optoelectronics, ultrafast science, ultra-high-frequency devices, optical data storage, and nanotechnology. Currently, he is head of the Institute for High Frequency and Quantum Electronics and Vicerector for Research at the University of Siegen, Siegen, Germany. He holds eight patents, five book contributions, and over 70 peer-review publications.

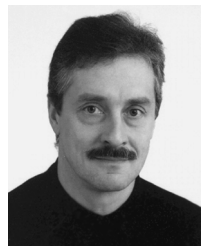

**Hartmut G. Roskos** studied physics at the Technical University of Karlsruhe and the Technical University of Munich; from the latter, he also received the Ph.D. degree in 1989 for a thesis on femtosecond spectroscopy in solid-state physics.

He then worked for two and a half years at AT&T Bell Laboratories, Holmdel, NJ. At that time, THz phenomena became a focus of his research. He later started a THz research group at the Institute of Semiconductor Electronics of RWTH Aachen. After receiving the Habilitation degree from RWTH Aachen with a thesis entitled "Coherent Phenomena in Solid-State Physics Investigated by THz Spectroscopy," he joined Goethe-University in 1997 as a Full Professor. Central themes of his group's research are THz physics and photonics, THz imaging, and the time-resolved optical and THz spectroscopy of inorganic semiconductors and organic compounds. In 2005, he spent a sabbatical at the University of California at Santa Barbara working towards a Bloch-gain THz laser. In 2009, OC Oerlikon AG awarded his group a five-year endowed Professorship for Terahertz Photonics. He spent the winter semester 2009–2010 as a Guest Professor at Osaka University's Institute of Laser Engineering performing THz spectroscopy on a one-dimensional organic metal.